LA-6529

C.3

UC-25

Issued: April 1977

Mechanical Properties of $^{238}PuO_2$

by

J. J. Petrovic
S. S. Hecker
C. C. Land
D. L. Rohr
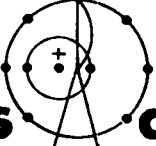
los alamos
scientific laboratory
of the University of California
LOS ALAMOS, NEW MEXICO 87545

MECHANICAL PROPERTIES OF ^{238}PuO$_2$

by

J. J. Petrovic, S. S. Hecker, C. C. Land, and D. L. Rohr

ABSTRACT

The mechanical properties of ^{238}PuO$_2$ have been examined in the Los Alamos Scientific Laboratory mechanical test facility built to handle α-radioactive materials. Compression tests were conducted as a function of temperature, strain rate, grain size, density, and storage time. At temperatures $\leq 1400°$C, test specimens of ^{238}PuO$_2$ exhibit pseudobrittle behavior due to internal cracks. Plastic deformation is "localized" at the crack tips. Generalized plastic deformation is observed at 1500°C. Ultimate stress values decrease markedly with increasing temperature and decreasing strain rate, and decrease less with decreasing density, increasing storage time, and increasing grain size. Room temperature fracture is transgranular, whereas intergranular fracture predominates at elevated temperatures. Crack-free specimens of ^{239}PuO$_2$ exhibit extensive plastic deformation at 1000°C and above. The relationship of these test results to the impact properties of ^{238}PuO$_2$ fuel in radioisotope thermoelectric generators is discussed.

I. INTRODUCTION

Radioisotope thermoelectric generators (RTG's) are used in space nuclear power systems and in some terrestial low-power systems. ^{238}PuO$_2$ is the most commonly used radioisotope fuel in the heat sources of space nuclear power systems. One of the primary safety requirements of such systems is that the highly radioactive and toxic ^{238}PuO$_2$ fuel be contained during accidents that might happen during launch pad aborts or Earth reentries. The container material must meet most stringent criteria such as compatibility with the fuel during operation, impact survival, and postimpact oxidation resistance.

The heat source for the current multihundred-watt RTG consists of twenty-four 37.2-mm-diam ^{238}PuO$_2$ spheres arranged in a cylinder (Fig. 1). Each sphere is clad with a 0.61-mm-thick Ir-0.3% W shell that is, in turn, surrounded by an 11.7-mm-thick graphite impact shell. This constitutes a fuel sphere assembly (FSA). The projected operating temperature for this system is ~1320°C. Potential Earth reentry can lead to 85-m/s impacts at 1440°C. Impact survival, defined as zero ^{238}PuO$_2$ release, depends not only on the properties of each individual FSA component (fuel, containment material, and graphite impact shell) but also on their relative properties. The graphite impact shell's effectiveness depends largely on the relative strengths of the fuel and graphite. Deformation of the containment material is governed by the fuel properties and the graphite impact shell. Very low-stength fuel leads to
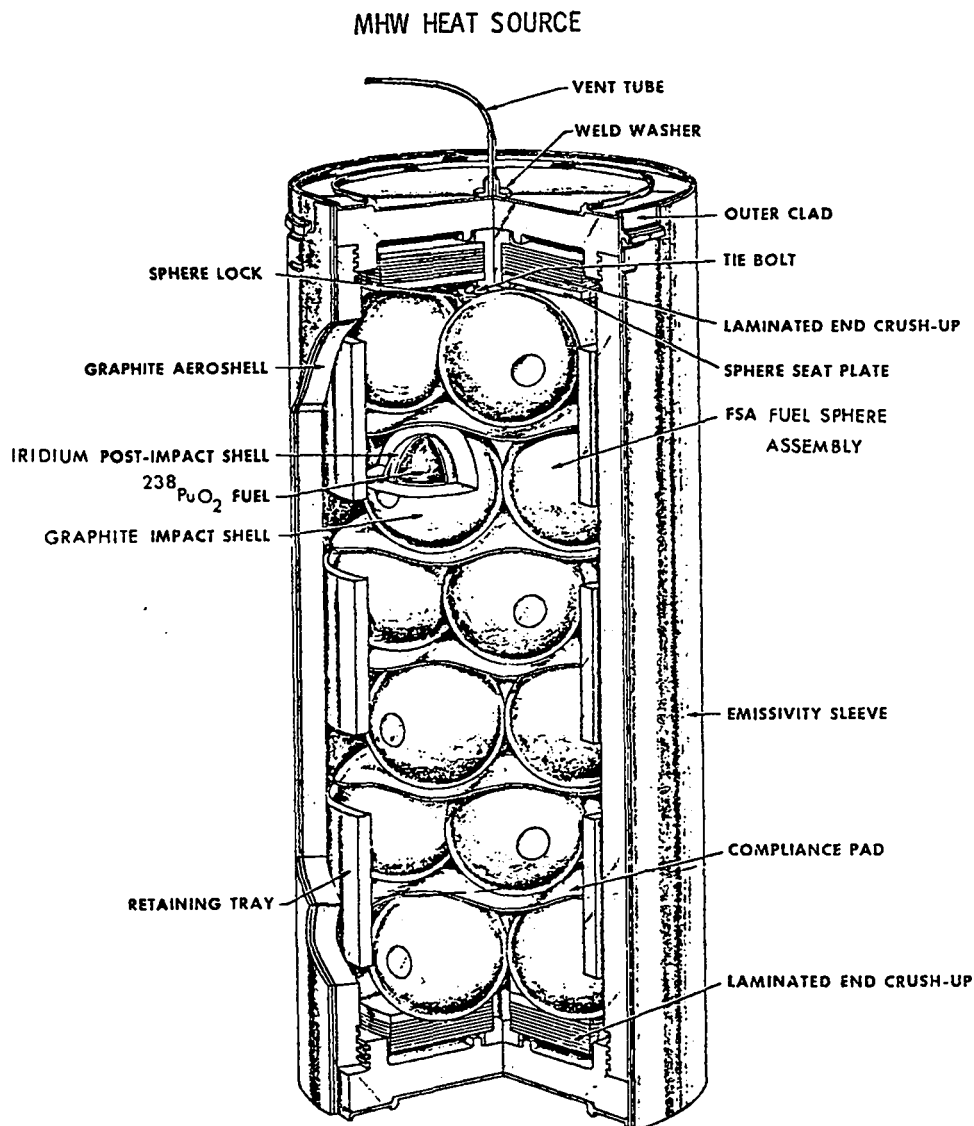
Fig. 1.

Multihundred-watt heat source for radioisotope thermoelectric generator built by General Electric's Space Division.

excessive hoop expansion of the sphere, whereas hard, brittle fuel may cause very high local bending strains.

Dynamic stress analysis of an FSA impact is being conducted at Fairchild Industries, Battelle Columbus Laboratories, and Los Alamos Scientific Laboratory (LASL). Although very sophisticated mechanics and numerical techniques are being used, no realistic material property data are available. The purpose of this investigation is to study the mechanical properties of $^{238}PuO_2$ at elevated temperatures. In addition to providing materials property input to stress analysis codes, we intend to relate these properties to the microstructure and then back to the fabrication processes. These properties should also help to define a suitable simulant for PuO_2 in impact tests required for safety verification and quality control.

There is virtually no $^{238}PuO_2$ mechanical property information in the literature. The thrust of our investigation has been to determine the properties of $^{238}PuO_2$ in uniaxial compression as a function of ambient to 1500°C temperature, low to moderate strain rate, and material structural variables such as density, grain size, and helium content with storage time. The results of these efforts and their bearing on the properties of $^{238}PuO_2$ fuel in RTG heat sources are discussed.

Appendix A presents PuO_2 fracture toughness parameters determined by the microhardness indentation technique. Appendix B shows additional metallographic results relevant to $^{238}PuO_2$ behavior. An expanded view (replica electron microscopy and scanning electron microscopy) of PuO_2 fractography is given in Appendix C. Annealing temperature's affect on $^{238}PuO_2$ microstructure is covered in some detail in Appendix D, and the annealing's affect on fracture surface topograpy is covered in Appendix E.

II. EXPERIMENTAL TESTING OF $^{238}PuO_2$

A. Test Facilities.

$^{238}PuO_2$ must be handled in glove boxes because of its high α radioactivity and toxicity. We designed and built a glove box facility for high-temperature mechanical testing of α-active materials (Figs. 2-3). It consists of three inert-atmosphere glove boxes and a transfer box. Two of the inert boxes are used for specimen preparation and measurement; the third contains a Centorr* high-temperature vacuum furnace (Fig. 4). This last box fits between the columns of an MTS** load frame. The Centorr furnace enclosure is welded to the back end of the glove box, so it forms part of the radioactive enclosure. Water-cooled stainless steel pull rods extend through stainless steel bellows into the furnace enclosure. Additional rubber bellows surround the stainless steel ones in case the latter break and release radioactive contamination. Outside the furnace, the pull rods connect to the load cell on top and to the hydraulic actuator on the bottom. Inside, they connect to spherical seats that permit connection to a

---

*Centorr Associates, Inc., Suncook, New Hampshire.

**Materials Test Systems, Inc., Minneapolis, Minnesota.

variety of mechanical testing fixtures such as the compression cage shown in Fig. 4.

The tungsten-mesh furnace is designed for operating temperatures as high as 2500°C. To date, we have conducted tests to 1500°C. There are two viewing ports in the furnace sides for optical pyrometers or optical extensometers. Temperatures during testing are typically measured by two Pt/Pt-10%Rh thermocouples placed in contact with the test specimen. A diffusion pumping system provides a vacuum of $<10^{-2}$ N/m^2 during elevated-temperature tests.

An MTS closed-loop electrohydraulic test system provides the loading capability. The hydraulic actuator can give up to 100-kN loads in tension or compression at displacement rates of $\sim 10^{-8}$ -170 mm/s. Servo-controlled electronics permit control of displacement, specimen load, or specimen strain. Thus we can run tests at constant load (creep) or at constant loading, strain, or displacement rate. Because of the extremely limited space inside the furnace chamber, we have not been able to build a suitable high-temperature extensometer. All high-temperature tests have, therefore, been displacement or load controlled. An LVDT transducer is used to measure ram displacement. Because we did not measure specimen strain directly, we could not get reliable elastic modulus measurements.

Test fixtures for high-temperature tests presented some difficulties because the long extension rods leading into the furnace cavity precluded direct compression tests. We used compression cages like the one shown in Fig. 4 which can be loaded in tension. The compression cage for service to 500°C was made of H-13 tool steel; the one for service above 500°C, of W-2% ThO_2. We have also designed fixtures for conducting four-point bending tests in the compression cages.

B. Materials.

Right circular cylindrical pellets for compression testing (Fig. 5) were fabricated by LASL Group CMB-11. Most were hot-pressed and sintered to length-to-diameter ratios of 1.0 or 1.5. Present techniques do not permit aspect ratios much different from these. Specimens were typically 7.5 mm in diameter by 7.5 or 12.5 mm long. All specimens
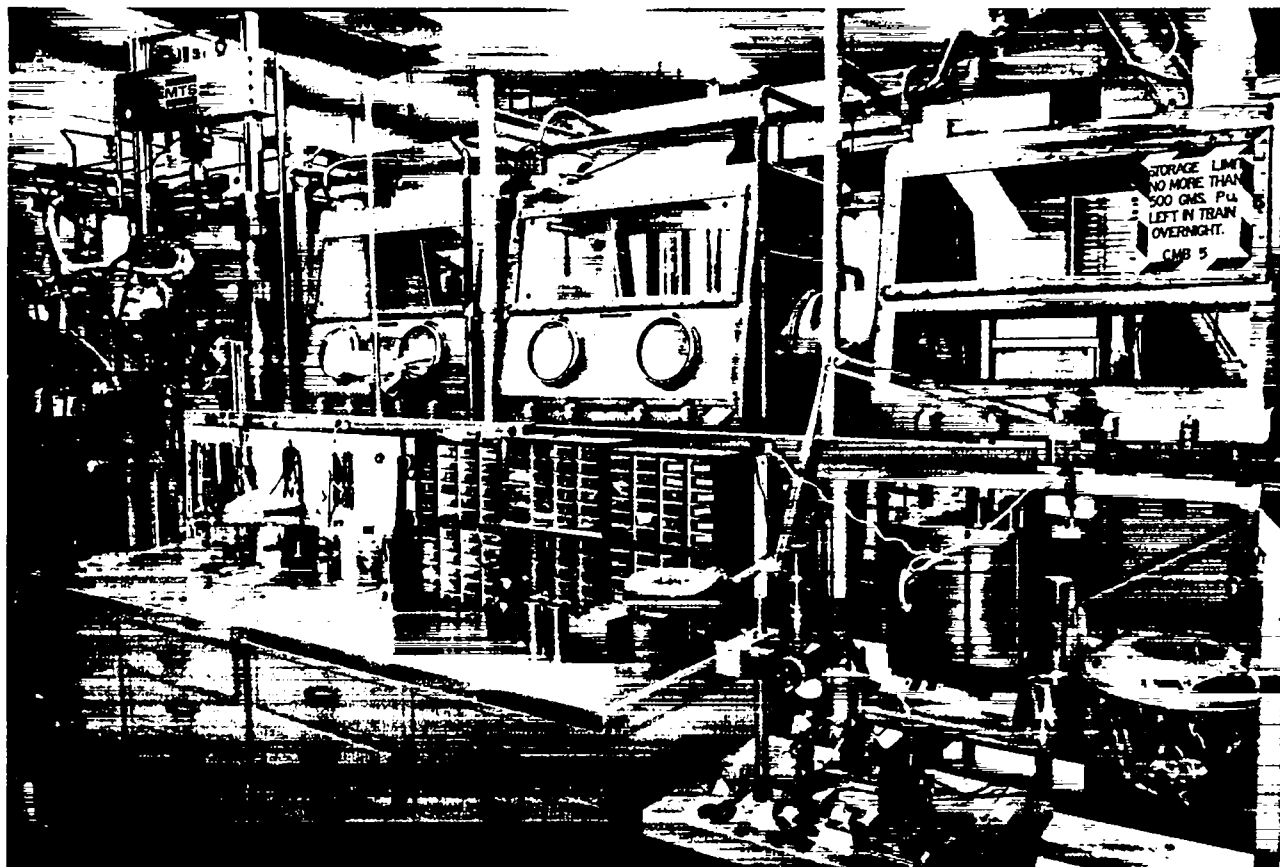
Fig. 2.
$^{238}PuO_2$ mechanical test facility showing inert glove-box train, Materials Test Systems, Inc. (MTS) load frame, and Centorr Associates, Inc., furnace.

had excellent dimensional tolerances as hot-pressed, so they required no machining. The flat ends of the pellets were parallel to within ±0.02 mm. Figure 6 shows the fabrication sequence for these pellets. We planned to study the mechanical properties of $^{238}PuO_2$ as a function of microstructure. For this initial work, we examined primarily the influence of density and grain size. To provide specimens with different grain sizes, we used a sintering temperature of either 1350 or 1530°C. The fabrication parameters for various material lots are detailed in Table I. Lot HPZ-390 was fabricated to a low density from special Savannah River feed. The other lots were all part of the LASL Group CMB-11 Prime Development Program. Typical chemical analyses are given in Table II.

$^{238}PuO_2$ produces α particles during radioactive decay which, in turn, form helium in the $^{238}PuO_2$ lattice. Helium accumulates continuously during ambient-temperature storage. When the temperature is raised above ~1000°C, the helium becomes mobile and migrates through the $^{238}PuO_2$ structure.[1] The heating rate and final temperature control the amount and type of microstructural damage produced by the helium migration.[1] Because of the helium generation, storage time becomes an important variable. The period between the sintering dates in Table I and the testing dates in Table III represents the storage time at ambient self-heating temperature, typically ~50°C. Storage times were 1 day-2 yr.
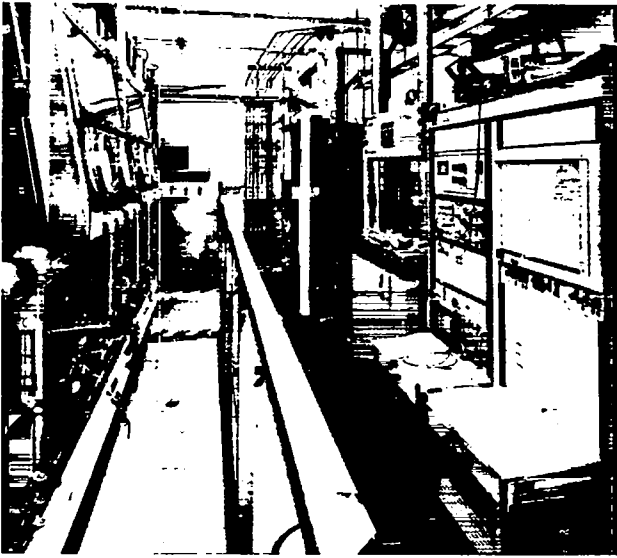
4

Fig. 3.

Inert glove-box train, MTS electrohydraulic control system, and Centorr furnace controls. Next to the MTS control console is an MTS load frame for nonradioactive materials testing.
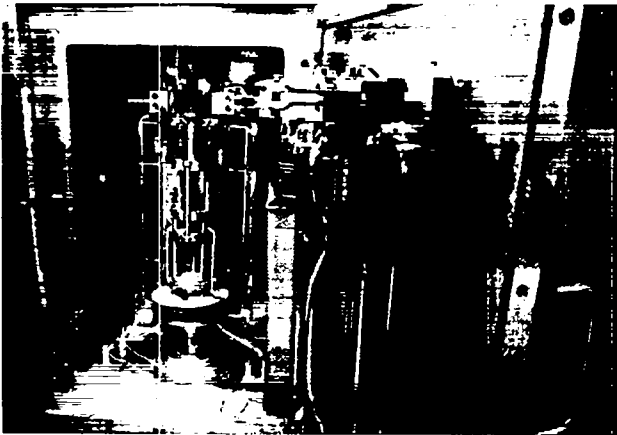

Fig. 4.

Centorr high-temperature vacuum furnace inside glove-box train. Compression test fixture for high-temperature (to 1500°C) testing is in place.
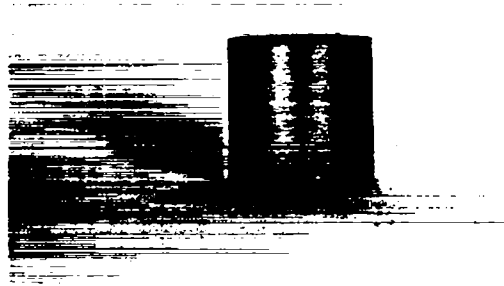

Fig. 5.

Typical as-fabricated ²³⁸PuO₂ compression test pellet. (2.5X).

238 PLUTONIA DEVELOPMENTAL PELLETS

RECEIVE SRP FEED

$H_2^{16}O$-Ar EXCHANGE   96 h at 775°C

OUTGAS   1 h at 1000°C

BALL MILL   32 h

2-μm FEED

COLD PRESS   ~60 TD

CRUSH AND   SCREEN TO SIZE   < 125 μm

$H_2^{16}O$-Ar SINTER   3 h at 1050°C

HOT PRESS   34.5 MPa for 20 min at 1530 °C

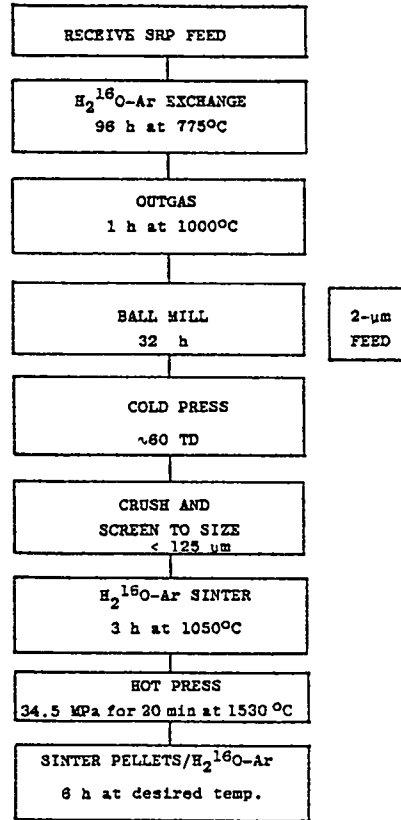| SINTER PELLETS/$H_2^{16}O$-Ar
 6 h at desired temp. |
| --- |

Fig. 6.

Fabrication flow-sheet for ²³⁸PuO₂.

TABLE I

$^{238}PuO_2$ MATERIALS

CMB-11 Code CMB-5 Code	Sinter Date	Feed	Hot-Pressing Conditions	Sinter Conditions	Grain Size (μm)	% Theoret Density
HPZ-390 14629	6/15/73	SRP direct strike	1440°C-30 min 34.5 MN/m²	1440°C 12 h	~12	78-79
HPZ-61 15211	3/27/74	LASL <125 μm	1530°C-20 min 34.5 MN/m²	1000°C 6 h 1350C 6 h	~12	90.7
HPZ-115 15714	2/26/75	LASL <125 μm	1530°C-20 min 34.5 MN/m²	1000°C 6 h 1527°C 6 h	16	92.3
HPZ-116 15715	2/26/75	LASL <125 μm	1530°C-20 min 34.5 MN/m²	1000°C 6 h 1350°C 6 h	12	92.1
HPZ-125 15805-6	5/28/75	LASL <125 μm	1530°C-min 34.5 MN/m²	1000°C 6 h 1350°C 6 h	~10	91

C. Compression Testing of $^{238}PuO_2$.

We tested $^{238}PuO_2$ compression pellets at temperatures from ambient to 1500°C with the apparatus described above. To prevent extensive spreading of $^{238}PuO_2$ fines within the test chamber during fracture, we designed a containment can for the compression pellets. The pellets were compressed between highly-polished tungsten platens while in the container. The container did not interfere with specimen deformation. The specimens were heated slowly to test temperature (typically 30- to 45-min heatup times) and tested at moderately low strain rates (Table III). Load vs ram displacement was recorded on an X-Y recorder.

III. $^{238}PuO_2$ COMPRESSION RESULTS

A. Macroscopic Results.

The test results are listed in Tables III and IV. The ultimate stress (derived from the maximum load) as a function of test temperature is plotted in Fig. 7. Shown for comparison is the 0.2% compressive yield stress of UO₂ that Radford and Terwilliger[2] recently determined using comparable density, grain size, and strain rate conditions. Ultimate stresses of ambient temperature $^{238}PuO_2$ are scattered from 45 to 510 MPa. By comparison, the ultimate stress[3] of room temperature UO₂ is 400-570 MN/m².

At temperatures as high as 1400°C, the $^{238}PuO_2$ was "brittle" in the sense that stress-strain curves were linear until near the ultimate stress, then rounded slightly before the specimen fractured catastrophically into small shards. In most cases, we could not define a 0.2% yield stress. In contrast, UO₂ exhibits 4-5% plastic strain[2] before fracturing at 1400°C. At 1500°C, there was generalized plastic deformation in the $^{238}PuO_2$, as is discussed later.

The $^{238}PuO_2$ ultimate stress was very temperature sensitive; the values roughly paralleled the temperature sensitivity of the UO₂ yield stress. However, all $^{238}PuO_2$ ultimate stress values were below the UO₂ yield stress values.

Figure 8 shows ultimate stress vs storage time at various temperatures. The ultimate stress decreased slightly, not markedly, with increasing storage time. Of special interest are the low storage time data at 1400°C. The specimens tested after 1-2 days of storage did not have significantly higher ultimate stresses, nor were they ductile. Thus, helium was not responsible for the "brittle" behavior observed in $^{238}PuO_2$.

TABLE II

PLUTONIA TEST PELLET SPECTROCHEMICAL ANALYSES

Element[a]	HPZ-61	HPZ-115	HPZ-116	HPZ-148
Al	45	75	50	20
B	<1	<1	<1	<1
Ba	4	4	7	<2
Be	<1	<1	<1	<1
Bi	<1	<1	<1	<1
Ca	280	370	320	100
Cd	<4	<4	<4	<10
Co	<1	<2	<2	<2
Cr	40	70	95	<5
Cs	<20	<20	<20	
Cu	2	4	4	<1
Fe	180	220	270	30
Hf	<4	<4	<4	<25
K	7	7	10	<5
La	<4	<4	<4	
Li	<4	<4	<4	<1
Mg	10	40	40	<2
Mn	5	6	7	1
Mo	10	20	35	<2
Na	<50	<50	<50	4
Nb	<10	<25	<25	<10
Ni	55	35	70	10
Pb	6	30	10	<5
Rb	<4	<4	<4	<10
Re	<4	<4	<4	
Si	260	130	130	60
Sn	<4	4	7	<5
Sr	<4	<4	4	<5
Ta	400	<100	270	<100
Ti	15	<10	<10	8
V	<1	<2	<2	<2
W	<10	<10	<10	25
Y	<4	<4	<4	
Zn	5	<5	<5	<5
Zr	<4	4	<4	<100

[a]Values expressed in parts per million. Spectrochemical analyses of lots HPZ-61, HPZ-115, and HPZ-116 were performed on as-fabricated pellets. Analysis of lot HPZ-148 was performed on powder feed material. Spectrochemical data are not available for Lots HPZ-390 and HPZ-125.

Storage of helium in the $^{238}PuO_2$ does alter the material's microstructure.[1] At 1400°C, formation of helium grain boundary bubbles was marked in specimens stored 50-400 days before testing. However, in the 1- to 2-day-old specimens, no helium bubbles were observed. At 1000°C, during the 45-min elevated temperature exposure in testing, optical metallography showed no appreciable helium grain boundary bubble formation. At 1500°C, diffusion rates in the $^{238}PuO_2$ are apparently high enough so that helium grain boundary voids coalesce into larger triple-point voids. Hence no grain boundary void stringers were observed.

TABLE III

$^{238}PuO_2$ COMPRESSION TESTS

Specimen	Test Date	Test Temp. (°C)	Strain Rate (s^{-1})	Deformation	Ultimate Stress (MN/m^2)
HPZ-390-1	4/15/74	~25	2.5 x 10^{-3}	Brittle[a]	65.9
HPZ-390-4	4/16/74	~25	2.5 x 10^{-3}	Brittle[a]	46.3
HPZ-390-5	4/16/74	~25	2.5 x 10^{-3}	Brittle[a]	129
HPZ-390-8	4/16/74	~25	2.5 x 10^{-3}	Brittle[a]	111
HPZ-390-9	4/16/74	~25	2.5 x 10^{-3}	Brittle[a]	73.3
HPZ-390-10	4/16/74	~25	2.5 x 10^{-3}	Brittle[a]	269
HPZ-390-11	2/24/75	1200	1 x 10^{-3}	Brittle[a]	41.2
HPZ-390-12	2/25/75	1200	1 x 10^{-3}	Failed during setup	---
HPZ-390-13	2/26/75	1200	1 x 10^{-2}	Brittle[a]	67.8
HPZ-390-14	2/27/75	1200	1 x 10^{-3}	Brittle[a]	36.8
HPZ-390-15	2/28/75	1400	1 x 10^{-3}	Brittle[a]	8.72
HPZ-390-16	3/03/75	1400	1 x 10^{-3}	Brittle[a]	12.0
HPZ-390-17	3/04/75	1400	1 x 10^{-3}	Brittle[a]	10.2
HPZ-390-18	3/05/75	1300	1 x 10^{-3}	Brittle[a]	16.0
HPZ-390-19	6/23/75	1400	1 x 10^{-3}	Brittle[a]	9.0
HPZ-390-20	6/24/75	1200	1 x 10^{-3}	Brittle[a]	42.4
HPZ-390-21	6/25/75	1400	1 x 10^{-3}	Brittle[a]	11.2
HPZ-390-22	7/17/75	1400	1 x 10^{-3}	Brittle[a]	11.8
HPZ-390-25	11/17/75	1000	1 x 10^{-3}	Brittle[a]	134
HPZ-61-1	8/22/75	~25	0.75 x 10^{-3}	Brittle[a]	335.
HPZ-61-3	11/14/75	1200	0.75 x 10^{-3}	Brittle[a]	90.3
HPZ-61-4	11/18/75	~25	0.75 x 10^{-3}	Brittle[a]	449
HPZ-61-5	4/03/75	1400	0.75 x 10^{-3}	Brittle[a]	28.4
HPZ-61-6	4/09/75	1400	0.75 x 10^{-3}	Brittle[a]	25.0
HPZ-61-7	4/10/75	1200	0.75 x 10^{-3}	Broke prematurely at chip	---
HPZ-61-8	4/11/75	1000	0.75 x 10^{-3}	Brittle[a]	166
HPZ-115-1	6/19/75	1400	0.75 x 10^{-3}	Brittle[a]	30.6
HPZ-115-2	8/28/75	~25	1.12 x 10^{-3}	Brittle[a]	290
HPZ-115-3	8/22/75	~25	1.12 x 10^{-3}	Brittle[a]	336
HPZ-115-5	11/13/75	1200	1.12 x 10^{-3}	Brittle[a]	73.8
HPZ-115-6	11/18/75	~25	1.12 x 10^{-3}	Brittle[a]	512
HPZ-115-7	11/10/75	1000	1.12 x 10^{-3}	Brittle[a]	189
HPZ-116-1	7/22/75	1400	0.75 x 10^{-3}	Brittle[a]	39.0
HPZ-116-3	7/21/75	1200	0.75 x 10^{-3}	Brittle[a]	101
HPZ-116-4	8/28/75	~25	0.75 x 10^{-3}	Brittle[a]	503
HPZ-116-7	4/23/75	1400	0.75 x 10^{-3}	Brittle[a]	46.2
HPZ-116-8	4/24/75	1000	0.75 x 10^{-3}	Brittle[a]	168
HPZ-116-9	8/27/75	~25	0.75 x 10^{-3}	Failed during setup	---
HPZ-116-10	8/28/75	~25	0.75 x 10^{-3}	Brittle[a]	336
HPZ-116-11	6/26/75	1400	0.75 x 10^{-4}	Brittle[a]	22.7
HPZ-116-12	7/02/75	~25	0.75 x 10^{-3}	Brittle[a]	507
HPZ-125-4	5/30/75	1400	1 x 10^{-3}	Brittle[a]	33.0
HPZ-125-4	8/21/75	~25	1 x 10^{-3}	Specimen still integral after 1400°C test	260
HPZ-125-5	5/29/75	1400	1 x 10^{-3}		41.6

[a]Load-deflection curves for test above 1000°C typically show slight rounding off before fracture, corresponding to 0.0018-0.0061 plastic strains. Room temperature tests show no rounding off before fracture.

TABLE IV

1500°C ^{238}PuO$_2$ COMPRESSION TESTS

Specimen	Test Date	0.2% Yield Stress (MN/m²)	Ultimate Stress (MN/m²)	Strain at Max. Load (%)	Final Strain (%)		Remarks
					Chart	Specimen	
HPZ-116-5 (15715-5)	11/19/75	4.92	9.40	1.16	4.38	7.57	Strain rate 7.44×10^{-4} S^{-1}
HPZ-116-6 (15715-6)	11/20/75	10.2	10.4	1.07	7.50	10.5	Strain rate 7.44×10^{-5} S^{-1} Accidentally preloaded past yield point
HPZ-115-8 (15714-8)	12/ 4/75	8.59	12.3	0.94	4.45	8.53	Strain rate 1.12×10^{-3} S^{-1}
HPZ-148-1 (16108-1)	12/ 2/75	7.67	16.5	1.42	6.74	7.29	Strain rate 1.12×10^{-3} S^{-1}
HPZ-61-9 (15211-9)	11/25/75	6.72	12.6	1.07	3.57	12.0	Strain rate 7.44×10^{-4} S^{-1}
HPZ-61-10 (15211-10)	11/26/75	0.44	---	---	---	2.61	Specimen deformed under weight of compression fixture only
HPZ-61-11 (15211-11)	12/01/75	8.02	8.02	0	6.79	8.30	Strain rate 7.44×10^{-5} S^{-1}
HPZ-61-13 (15211-13)	12/12/75	1.54	2.42	2.81	8.13	8.24	Strain rate 7.44×10^{-6} S^{-1}
HPZ-61-15 (15211-15)	12/16/75	---	35.4	0.09	---	---	Strain rate 7.44×10^{-3} S^{-1} Brittle fracture Specimen shattered into many shards,

6
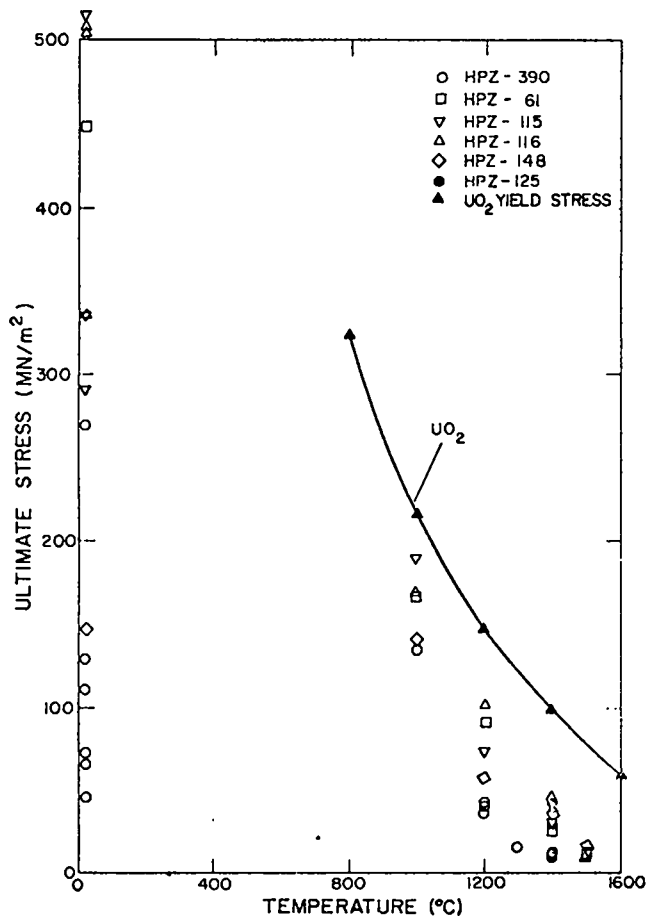
Fig. 7.

$^{238}PuO_2$ compressive ultimate stress vs test temperature, for various material conditions. The 0.2% yield stress of UO_2 is shown for comparison. The ultimate stress is very temperature sensitive.

Fig. 8.

$^{238}PuO_2$ compressive ultimate stress vs ambient-temperature (~50°C) storage time at various test temperatures. Ultimate stress values decrease only slightly with increasing storage time.

Figure 9 shows the effect of density on ultimate stress at various temperatures. As would be expected of a ceramic material, the ultimate stress increased with increasing density.

Figure 10 shows ultimate stress vs grain size for the 12- and 16-um grains tested to date. At the higher temperatures, the ultimate stress tended to decrease with increasing grain size, although the effect was not marked and seemed to disappear at 150-0°C. There was a possible reversal of grain size trend at 1000°C, but this effect may simply reflect statistical scatter in strength values.

Figure 11 shows the effect of strain rate on ultimate stress in the $^{238}PuO_2$. Unlike grain size and storage time variations, strain rate strongly affected the ultimate stress. The ultimate stress approximately doubled with a tenfold increase in strain rate.

We have shown that $^{238}PuO_2$ appears to exhibit brittle behavior at high temperatures, but does not exhibit other features usually assumed typical of brittleness. The ultimate strength of PuO_2 is highly dependent on both temperature and strain rate. Large temperature and strain rate sensitivity is usually taken to indicate involvement of a plastic deformation process in the fracture mechanism. Also, UO_2, a material of the same crystal structure which is completely miscible with PuO_2, exhibits plastic deformation readily in the temperature range where the $^{238}PuO_2$ is "brittle." This is so although UO_2 has a higher melting point than $^{238}PuO_2$. In fact,

10
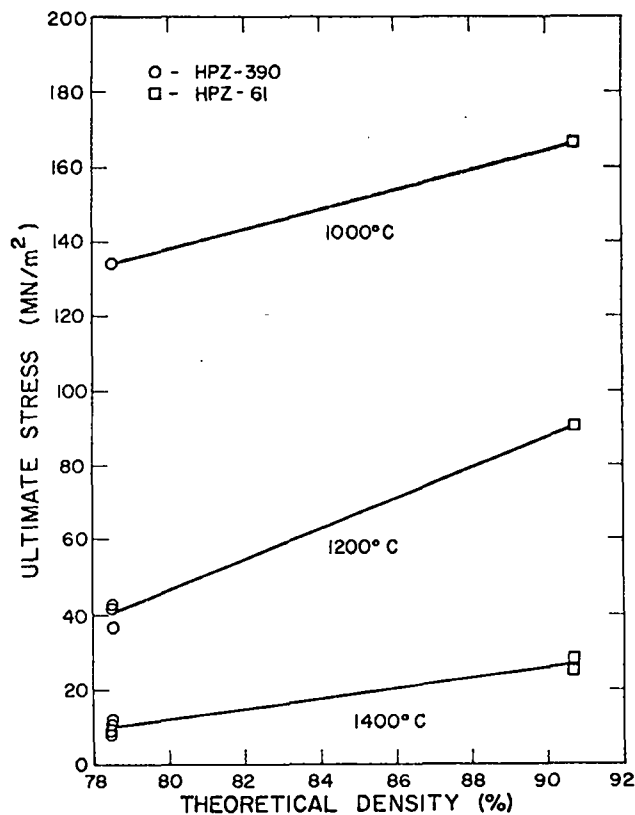
Fig. 9.
$^{238}PuO_2$ compressive ultimate stress vs %
theoretical density, at various test
temperatures. Stress values increase with in-
creasing density.
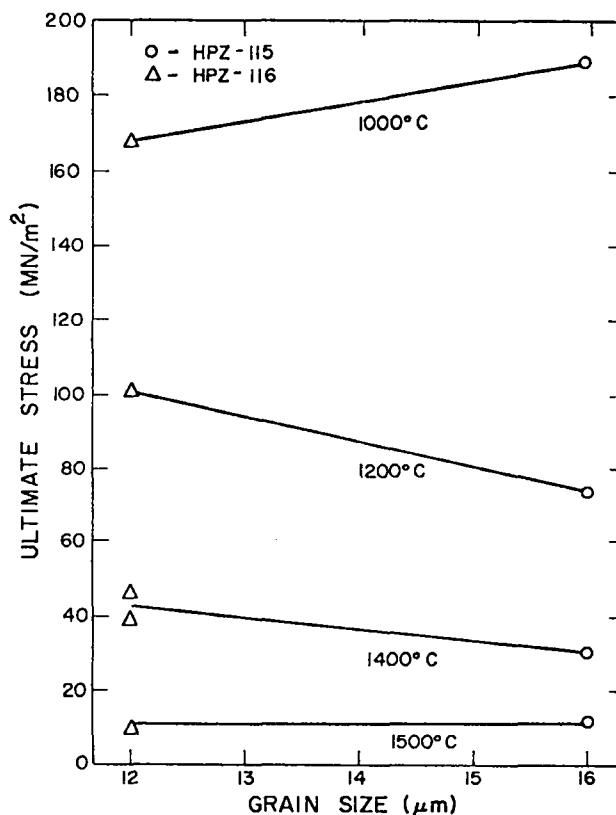
Fig. 10.
$^{238}PuO_2$ compressive ultimate stress vs grain
size, at various test temperatures. The
ultimate stress is not a marked function of
grain size, decreasing only slightly with in-
creasing grain size at the higher temperatures.

UO_2 exhibits yield stress temperature and strain
rate sensitivities very similar to those observed for
the ultimate stress[2] in $^{238}PuO_2$.

Thus, $^{238}PuO_2$ really behaves in a pseudobrittle
manner, in that the response appears brittle from
stress-strain curves, but does not have the
characteristics of true brittle fracture. Figure 12
shows what we believe to be the cause of the
pseudobrittle behavior observed up to 1400°C. This
section 3.2 mm from the end of an as-fabricated test
pellet of Lot HPZ-116 shows a network of fine inter-
nal cracks which represents a three-dimensional
crack network in the test specimen. Thus, this pellet
was not integral as-fabricated. Radiography of this
specimen failed to reveal these cracks, indicating
that this method's resolution was inadequate.
Similar crack patterns also were observed in as-
fabricated specimens of Lots HPZ-61 and HPZ-115,
suggesting that all test specimens to date had such
internal cracks, as they were all fabricated under
similar conditions.

When cracks of the type shown in Fig. 12 are
loaded in compression, stress is concentrated at
their tips. At elevated temperatures, plastic defor-
mation starts at the crack tips because of these
stress concentrations. Thus, instead of being
generalized, the plastic deformation is "localized" at
the crack tips. This plastic deformation, which may
be extensive locally, causes the cracks to extend,
leading to a slight observable plastic deformation
before catastrophic fracture of the specimen, which
is exactly what was observed. Possibly, the presence
of the cracks may have masked true effects of
material variables such as storage time and grain
size on the mechanical properties.

11
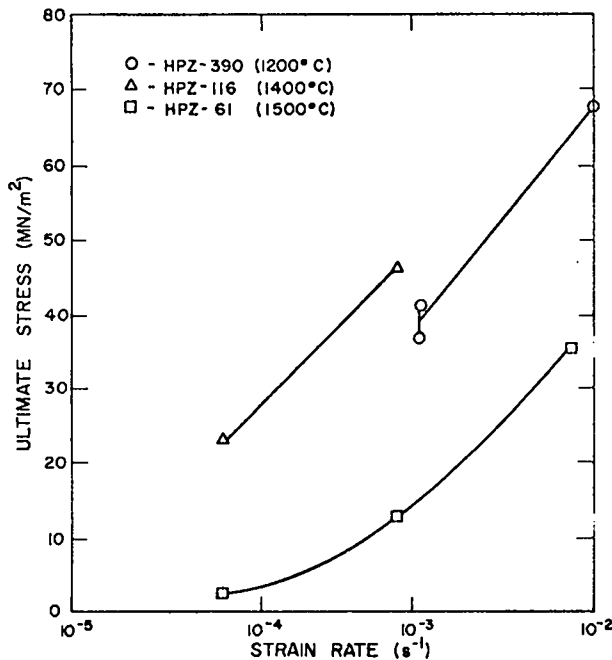
Fig. 11.

$^{238}PuO_2$ *compressive ultimate stress vs strain rate, at various test temperatures. Ultimate stress levels are highly strain rate sensitive, increasing with increasing strain rate.*

Fig. 12.
As-fabricated test pellet of Lot HPZ-116, sectioned approximately 3.2 mm into its interior and showing a network of large internal cracks. (10X).

This rationale would account for the temperature dependence of the ultimate stress, which would be controlled by the temperature dependence of the local plastic deformation. It would also account for the strain rate dependence. At lower strain rates, more local plastic deformation could occur, leading to increased crack extension before fracture and to a consequently lower ultimate stress.

The above rationale assumes that local plastic deformation in $^{238}PuO_2$ begins at a relatively low temperature, probably not too different from initiation of plastic deformation in UO_2. This low temperature might be estimated by observing the temperature at which the $^{238}PuO_2$ ceases to exhibit strain rate sensitivity of the ultimate stress. Recent experiments suggest that $^{238}PuO_2$ is not strain rate sensitive at 800°C.

The above explanation suggests that general plastic deformation would be observed in $^{238}PuO_2$ below 1500°C, if the specimens tested were free of internal cracks. Because all the specimens we tested apparently contained cracks before testing, general

plastic deformation might be observable only at higher temperatures, at which plastic deformation could occur at very low stress levels. In fact, this was the case.

Table IV lists the results of the various tests at 1500°C. Figure 13 shows engineering stress-strain curves for specimens of Lot HPZ-61 tested at 1500°C at various strain rates. At the highest strain rate, the pseudobrittle behavior was observed. The stress-strain curve is linear, with slight rounding at the ultimate stress, followed by the sample's catastrophic fracture into shards. A 0.2% yield stress cannot be defined. However, at the lower strain rates, generalized plastic deformation was observed and the 0.2% yield stresses can be defined. The yield stresses and ultimate stresses decreased with decreasing strain rate. At the lowest strain rate, there was an apparent decrease in the modulus. Fracture was no longer catastrophic at the lower strain rates. The stress dropped off gradually beyond the point of maximum load. The total amount of plastic strain increased with decreasing strain rate. At the lowest strain rate, we observed 8% plastic strain, quite large for a ceramic material.
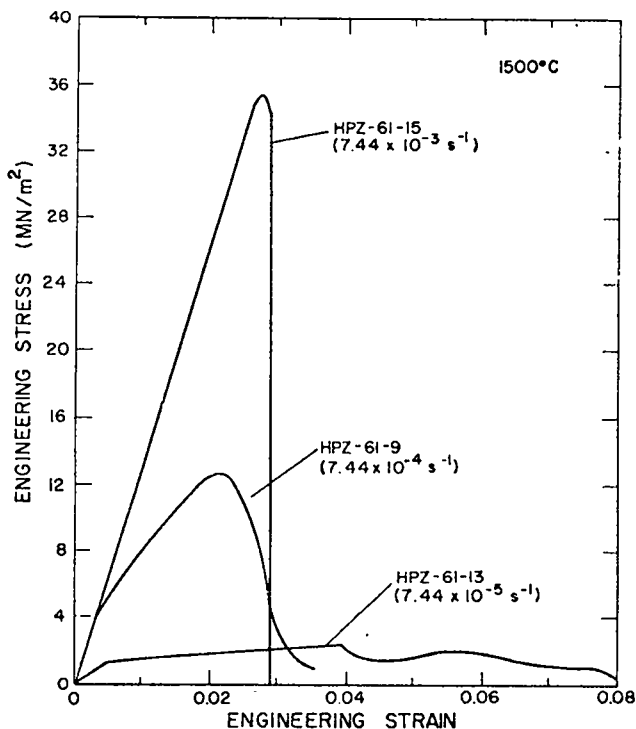
Fig. 13.
Engineering stress-strain curves at 1500°C, for specimens from Lot HPZ-61. Elastic strains are the sum of both the specimen and load train. Assuming a modulus of 3.45 x 10⁴ MN/m² at 1500°C, elastic strains in specimen HPZ-61-15 would be of the order of 0.001 near the ultimate stress.

The detail in the stress-strain curve at the lowest strain rate is probably due to the slow displacement of cracks. All the characteristics of these 1500°C tests are representative of large-scale plastic deformation in the $^{238}PuO_2$.

Figure 14 shows specimen HPZ-61-13 tested at 1500°C. Although this specimen exhibited 8% plastic strain before the stress went to zero, it was still largely sound. There was some barrelling and chipping and a large surface crack, but the specimen did not fracture catastrophically into small shards, as happened at 1400°C and below.
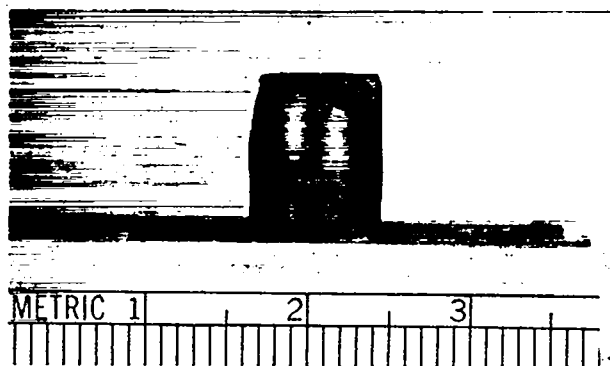
Fig. 14.
Specimen HPZ-61-13, after test at 1500°C. The test pellet has not shattered into many small shards. Note the chip and large surface crack.

B. Microstructural Characteristics of Deformation.

Figure 15 is a metallographic section of a $^{238}PuO_2$ specimen fractured at room temperature. The microstructures of as-fabricated $^{238}PuO_2$ typically showed internal grain porosity, triple-point pores, and some pores along the grain boundaries. The room temperature fracture was totally transgranular with cracks traversing the grains. Figure 16 is a replica electron micrograph of the room-temperature transgranular fracture. Fracturing has exposed the internal grain porosity, and cleavage markings are evident.

Elevated-temperature exposure can lead to formation of grain boundary helium bubbles in $^{238}PuO_2$.[1,4,5] The grain boundary helium effects were not prominent in a specimen of Lot HPZ-61, tested at 1000°C 374 days after fabrication, as Fig. 17 shows. The specimen was held at temperature ~45 min. The grain boundary structure was the same as that of material that had never been exposed to high temperature. However, Figure 18 shows that HPZ-61 tested at 1400°C, 366 days after fabrication, formed an extensive network of grain boundary

Fig. 15.

Specimen HPZ-115-3, tested at ambient temperature. The transgranular fracture mode is operative, and cracks traverse grains and grain boundaries. (1000X).

helium bubbles. Stringers of bubbles may be seen at nearly all the grain boundaries. At 1500°C, however, the stringers of grain boundary helium bubbles disappeared, being replaced by agglomerations of larger voids, as shown in Fig. 19. Apparently, at 1500°C, diffusion rates were high enough to allow the grain boundary bubbles to agglomerate, leaving relatively clean grain boundaries.

The effects of grain boundary helium bubble formation on the mechanical properties of $^{238}PuO_2$ are not clearly established because of the cracks in the as-fabricated test pellets. The effect of the cracks may overide the influence of grain boundary bubbles. Certainly, if $^{238}PuO_2$ deformation occurs by a grain boundary sliding mechanism, one would expect an effect from the grain boundary helium bubbles. However, a clear-cut description of this influence must await testing of sound material.

Figure 20 shows a polished longitudinal cross section of specimen HPZ-61-13 tested at a low strain rate at 1500°C, the stress-strain curve for which is shown in Fig. 13. This specimen exhibited about 8% plastic strain, as determined from measurements of its length before and after testing. Note that, even after this amount of strain, the specimen was sound enough to endure the mounting and polishing procedures required to obtain the longitudinal section. Some of the cracks were probably present before testing.

Some aspects of the $^{238}PuO_2$ deformation process are shown in Fig. 20. Radial bulging of the specimen is apparent at the midsection. Deformation appeared to be taking place along 45° directions, resulting in some cavitation along these directions as well as in the center of the specimen. A large crack has developed along one of the 45° deformation directions. These 45° directions are the directions of maximum shear stress in the compression test, and any deformation resulting from a dislocatton mechanism or grain boundary sliding would be expected to be maximized in these directions.

Figure 21 shows the structure adjacent to large cracks in the $^{238}PuO_2$ after elevated temperature fracturing, as near the cracks along the 45° directions in Fig. 20. Extensive areas of intergranular separations are found near the cracks. The number of intergranular separations decreases away from the cracks, suggesting that these separations play a role in formation and propagation of large cracks at elevated temperature.

More detailed intergranular separation is shown in Fig. 22. In this region, the grain boundaries are almost completely separated. The following questions arise. How and when do these grain boundary separations form during plastic deformation of $^{238}PuO_2$? Are they the end result of a large amount of continuous local plastic deformation, or do they form early during the plastic deformation process? In other words, is the material deforming continuously or discontinuously?

These questions cannot be answered precisely for $^{238}PuO_2$ at present. For the cracks shown in Fig. 22, the strains represented by the cracked regions in relation to the grain size are about 10%. This might suggest extensive prior continuous deformation. Note that both UO_2 and ThO_2, materials similar to $^{238}PuO_2$, exhibit grain boundary separations as a result of elevated temperature deformation.[6-10] In both of these materials, continuous deformation seems to precede formation of intergranular separations. Such intergranular separations in ceramic
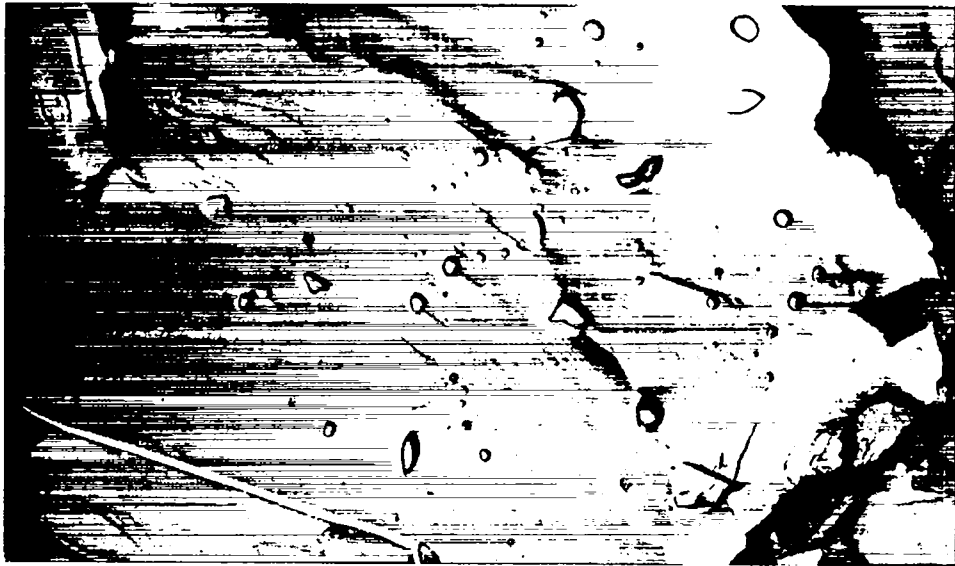
14

Fig. 16.

Replica electron micrograph of ambient temperature $^{238}PuO_2$ fracture surface. Transgranular fracture has produced cleavage steps and has exposed internal grain porosity. (4000X).
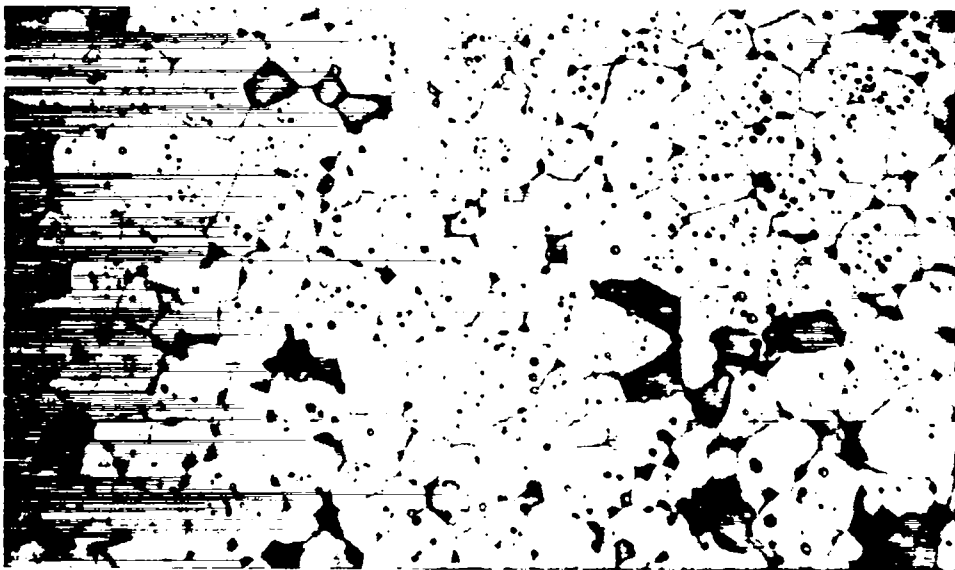

Fig. 17.

Specimen HPZ-61-8, tested at 1000°C. Grain boundary helium bubbles are not prominent after this temperature exposure. The grain boundary structure appeared the same as in the as-fabricated specimen. (1000X).
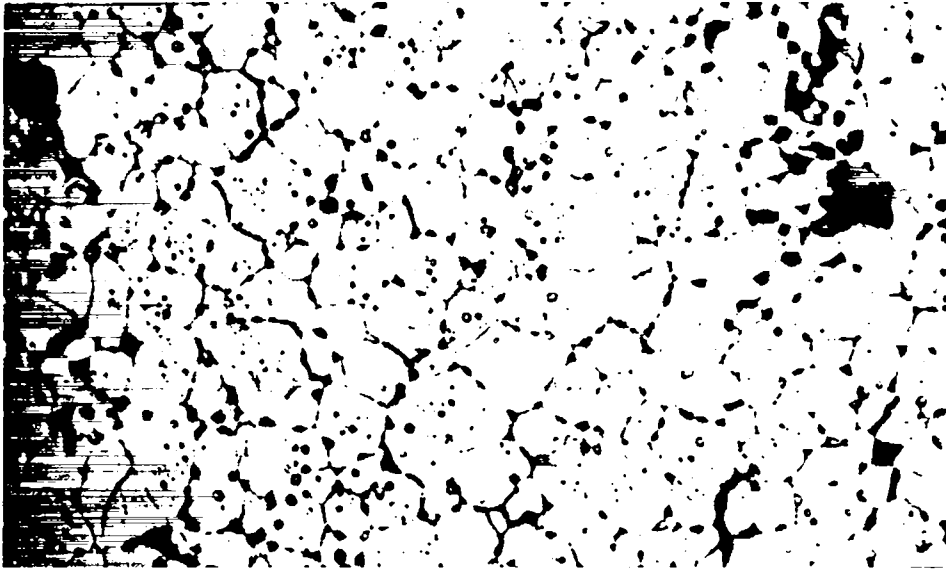
Fig. 18.

Specimen HPZ-61-5, tested at 1400°C. Grain boundary helium bubble stringers are very prominent after this temperature exposure. (1000X).

Fig. 19.

Specimen HPZ-61-13, tested at 1500°C. The grain boundary helium bubble stringers have disappeared, being replaced by larger voids. (500X).

Fig. 20.
Polished cross section of specimen HPZ-61-13, tested at 1500°C. Note the radial bulging, and cavitation along 45° deformation directions. Probable as-fabricated cracks also evident. (6X).

materials usually denote a grain boundary sliding mode of deformation. Figure 23 is a replica electron micrograph of these intergranular separations in $^{238}PuO_2$. Grain boundary helium bubbles at the areas of separation are apparent.

Figure 24 shows that dislocations are present in the $^{238}PuO_2$ after deformation at 1400°C. The extent of the dislocations' contribution to plastic deformation of $^{238}PuO_2$ has not yet been determined. However, dislocation motion contributes to deformation of polycrystalline UO_2 at elevated temperatures.[11]

IV. PLUTONIA-239 MECHANICAL PROPERTIES

We have tested plutonia-239 and the results may have a significant bearing on understanding and improving the elevated temperature deformation responses of $^{238}PuO_2$.

A. Specimen Fabrication Conditions.

A plutonia (HPZ-148) was fabricated by hot pressing and sintering as outlined for $^{238}PuO_2$ in Fig. 6. After hot pressing, the material was substoichiometric, with an O/Pu ratio of approximately
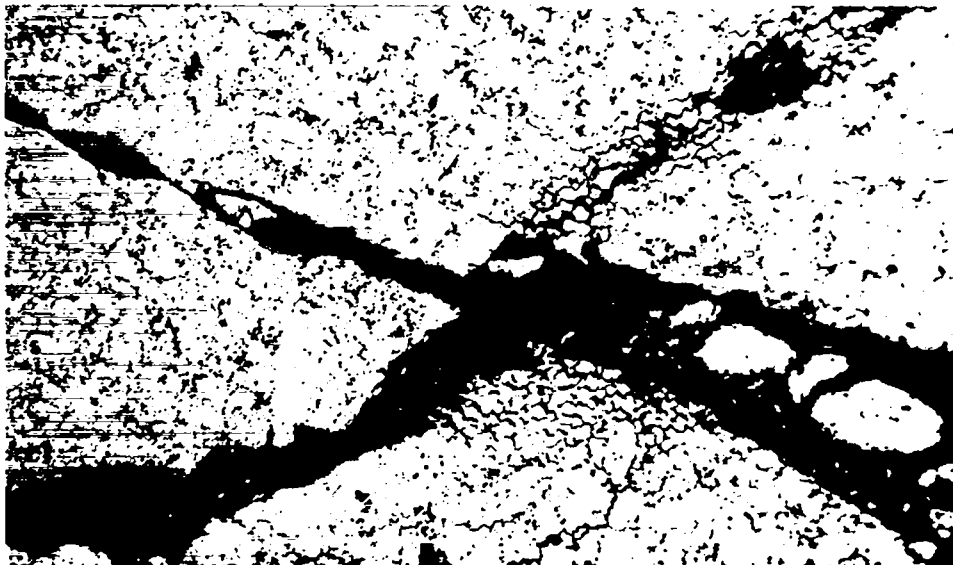
Fig. 21.
Specimen HPZ-116-7, tested at 1400°C. Intense intergranular fracture occurs adjacent to large cracks. Note the decreased intensity of the intergranular separations away from the immediate vicinity of the large cracks. (100X).

17
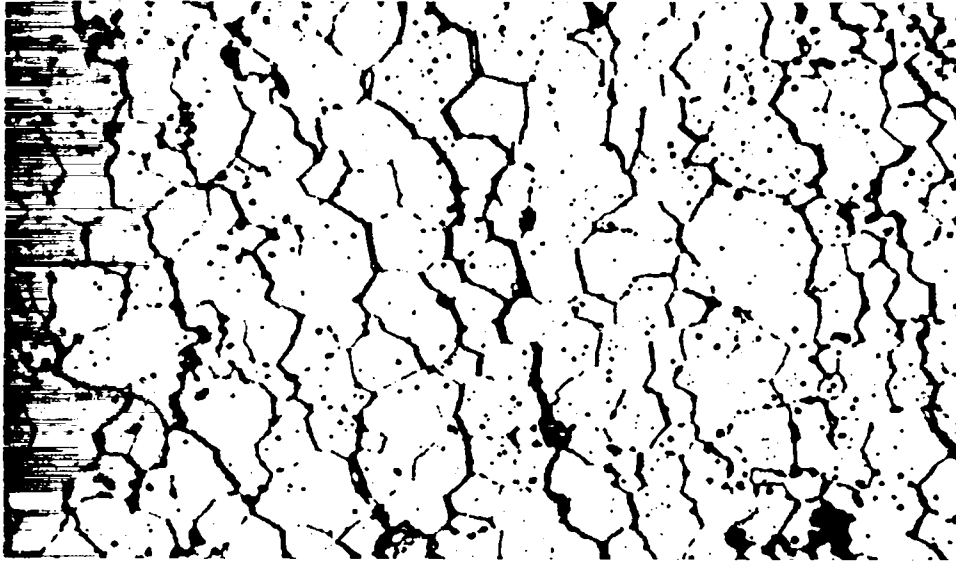
Fig. 22.

Specimen HPZ-61-5, tested at 1400°C. The grain boundaries are almost totally separated in this region of the specimen. (500X).

Fig. 23.

Replica electron micrograph of the fracture surface of specimen HPZ-116-8, tested at 1000°C. Intergranular fracture has delineated the grains and exposed grain boundary porosity. (4200X).

Fig. 24.
Transmission electron micrograph of specimen HPZ-61-5, after test at 1400°C. Dislocations are observed in $^{238}PuO_2$ after mechanical deformation. (60 000X).

1.88. Two pellets from the lot, HPZ-148-14 and HPZ-148-15, were not sintered subsequently. The rest were sintered for 6 h at 1000°C plus 6 h at 1350°C in Ar-H$_2^6$O. The as-hot pressed specimens were 86% dense; the sintered ones were 87% dense. The plutonia-239 grain size was approximately 15 μm. Fabrication conditions for the plutonia-239 were the same as those for $^{238}PuO_2$ Lots HPZ-61, -116, and -125.

Figure 25 shows a ground plutonia-239 pellet that was hot pressed, but not sintered. This pellet did not contain internal cracks but was substoichiometric, with an O/Pu ratio of approximately 1.88. Figure 26 shows that when this uncracked material was sintered, the internal crack structure developed. Thus, the internal cracking occurs during the sintering sequence. The two most likely explanations are internal stresses resulting from the reoxidation process and thermal shock effects. The exact cracking mechanism is unknown, but definitive experiments are in progress to determine the origin and eliminate the cracking.

B. Compression Test Results.

Compression test results for the plutonia-239 are detailed in Table V. The presence or absence of internal cracks in the plutonia-239 test pellets (Figs. 25 and 26) can profoundly influence the macrosopically observed mechanical properties. Figure 27 shows engineering stress-strain curves for plutonia-239 both as-hot pressed and after sintering at 1000°C The sintered material behaved in the same pseudobrittle manner as $^{238}PuO_2$. However, the as-hot pressed material showed large-scale plastic deformation. The test was terminated after 16% strain. The yield stress of the as-hot pressed material was higher than the ultimate stress of the sintered material. The reason for the rather large modulus difference between these two material conditions may be the crack network in the sintered specimen.

The difference between strength levels and ductility was even more striking at 1200°C, as shown in

19
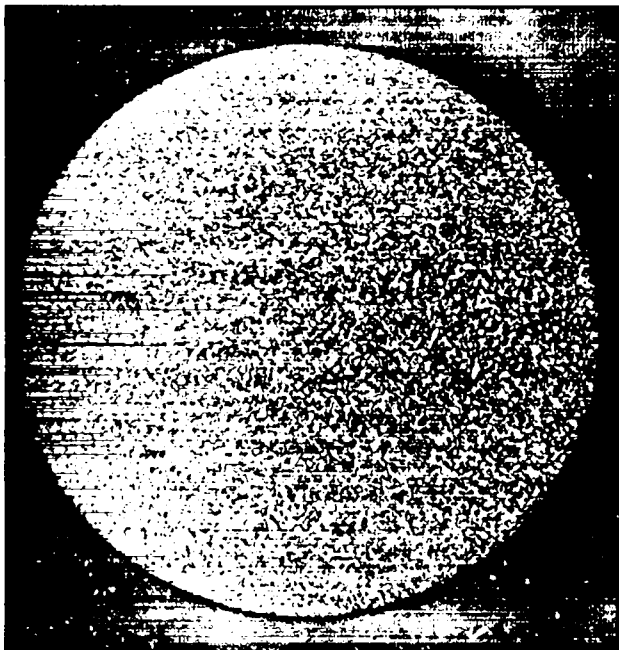
Fig. 25.
As-hot pressed pellet of plutonia-239, sectioned approximately 3.2 mm into its interior. At this stage in the fabrication processing, the pellet is free of large internal cracking. (10X).
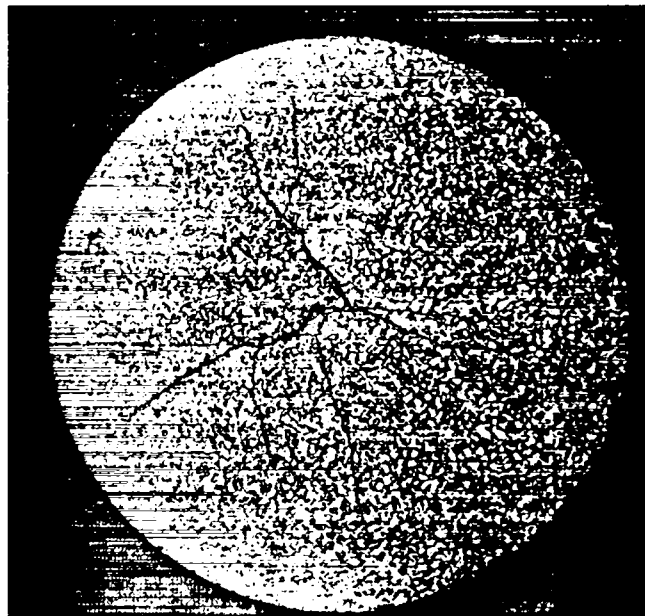
Fig. 26.
Hot-pressed and sintered pellet of plutonia-239, sectioned approximately 3.2 mm into its interior. Sintering has produced fully stoichiometric material (O/Pu ratio of 2.00) and large cracks. (10X).

Fig. 28. The as-hot-pressed test was terminated after 14% strain.

Figure 29 compares the yield stresses obtained in the as-hot pressed plutonia-239 with the comparable UO_2 data.[2] Although the plutonia-239 values are lower than the UO_2 values, the temperature dependence of the yield stress is similar to that of UO_2.

C. Microstructural Characteristics of Deformation.

Figure 30 compares the as-hot pressed plutonia-239 pellet tested at 1200°C with an untested one. The tested pellet has undergone considerable axial straining and has barrelled radially. This pellet was very sound after testing and exhibited no surface cracking. Figure 31 shows a polished cross section of this specimen. There is no visible cracking in the cross-sectional view. Figure 32 shows the microstructure of the pellet interior at higher

magnification. The compression direction is vertical. There is some suggestion that the individual granules in the microstructure have become flattened in that direction, indicating large amounts of plastic deformation. Etching (Fig. 33) showed the microstructure to be a two-phase mixture of $PuO_{1.62}$ (dark phase) and $PuO_{1.98}$ (light phase), as would be expected at room temperature in substoichiometric material. At test temperature, however, the material was single-phase. The formation of the second phase during cooling prevented resolution of the grain boundary structure.

Figure 34 is a macrograph of the plutonia-239 as-hot pressed specimen tested at 1000°C. After 16% strain, the specimen was very barrelled and had developed a large crack, perhaps because of the barrelling. A polished cross section of the specimen is shown in Fig. 35. The large crack extends radially into the specimen, but no other cracking is apparent. Figure 36 shows the tip of the large crack at high magnification. The crack tends to run across the granules of the microstructure. Because of the

TABLE V

^{239}PuO$_2$ COMPRESSION TESTS

Specimen	Test Temp (°C)	Strain Rate (s⁻¹)	0.2% Yield Stress (MN/m²)	Ultimate Stress (MN/m²)	Strain at Max. Load	Final Strain (%)		Remarks
						Chart	Specimen	
HPZ-148-2 (16108-2)	1000	1.12 x 10⁻³	137	140	0.51%	---	---	Specimen shattered.
HPZ-148-3 (16108-3)	1200	1.09 x 10⁻³	56.4	57.3	0.39%	---	---	Specimen half shattered.
HPZ-148-4 (16108-4)	1400	1.12 x 10⁻³	24.3	35.5	2.48%	8.46%	6.27%	Specimen exhibited plastic deformation.
HPZ-148-14 (16108-14)	1200	1.12 x 10⁻³	126	---	---	13.9%	14.1%	Specimen deformed extensively. Test terminated at 14% strain.
HPZ-148-15 (16108-15)	1000	1.11 x 10⁻³	188	---	---	16.3%	16.9%	Specimen deformed extensively. Test terminated at 16% strain.
HPZ-148-6 (16108-6)	~25	1.11 x 10⁻³	146	146	---	---	---	Brittle fracture
HPZ-148-1 (16108-1)	1500	1.12 x 10⁻³	7.67	16.5	1.42%	6.74%	7.29%	Specimen exhibited plastic deformation.

material's two-phase structure, we could not determine whether this cracking was transgranular or intergranular.

D. Implications of the Plutonia-239 Results.

The as-hot pressed plutonia-239 specimen results suggest that ^{239}PuO$_2$ specimens without internal cracks may exhibit large amounts of macroscopic plastic deformation considerably below 1500°C. Possibly, the substoichiometric character of the as-hot pressed plutonia-239 specimens may have enhanced their propensity for plastic deformation. Certainly, such enhancement occurs in UO$_2$ and UO$_2$-PuO$_2$ mixed oxides.[12] However, stoichiometry effects on plasticity in the plutonia are believed to be secondary to the effects of the observed internal cracks.

V. ^{238}PuO$_2$ PROPERTIES IN HEAT SOURCES

The ^{238}PuO$_2$ fuel used in the multihundred-watt RTG heat source is fabricated at Mound Laboratories (Monsanto Research Corporation). The average fuel density is ~83%, with considerable variation within a sphere, as shown in Fig. 37. All spheres received and tested at LASL were typically cracked as shown in Fig. 38. Cramer[13] noted that the spheres were cracked (although most were still intact), whether or not they were intentionally vibrated at Mound Laboratories. The origin of these macroscopic cracks is not clear.

LASL has impact tested many individual FSA's as part of a series of safety qualification tests. Cramer[13,14] has summarized the results of many of these tests. Two types of behavior have been observed in the ^{238}PuO$_2$ fuel: predominantly brittle
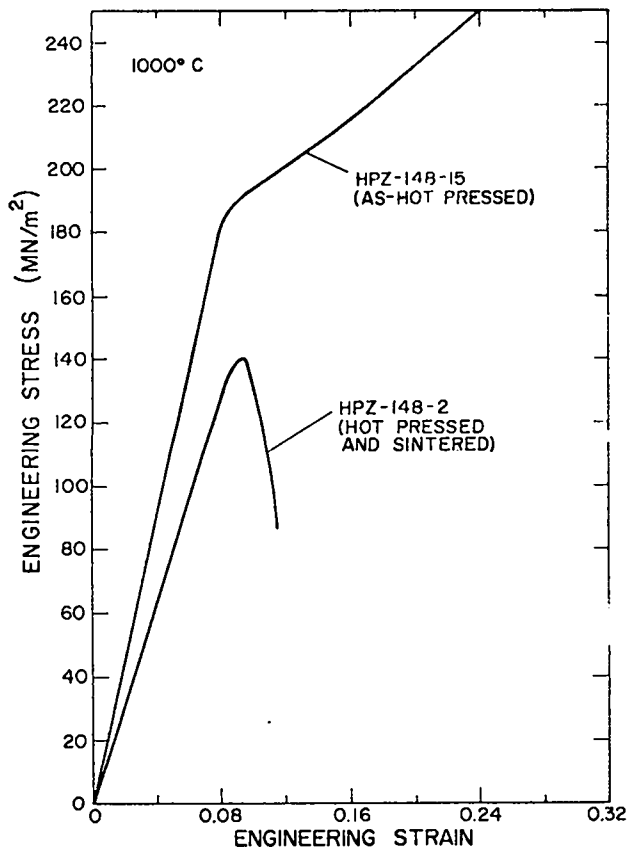
Fig. 27.

Engineering stress-strain curves at 1000°C in as-hot pressed and hot-pressed and sintered plutonia-239. Elastic modulus values are apparent, because they contain both specimen and load train elastic displacements. Large cracks in the test pellets drastically reduce the microscopically observed ductility, and lower strength levels.

Fig. 28.

Engineering stress and strain curves at 1200°C in as-hot pressed and hot-pressed and sintered plutonia-239. Elastic modulus values are apparent, because they contain both specimen and load train elastic displacements.

fracture and crushing with extensive fines generation (Fig. 39), and pronounced plastic flow with little cracking and fines generation (Fig. 40). We do not yet understand the reasons for these differences.

The descriptions of the fuel's mechanical properties for these two types of behavior are necessarily quite different. For the brittle behavior, fracture is preceeded by elastic deformation until a macroscopic fracture stress is exceeded, at which point crushing takes place, as the fuel is contained in the iridium shell. The ultimate strengths of the $^{238}PuO_2$ pellets tested are our best estimate of a macroscopic fracture stress. These results are plot-

ted as a function of test temperature in Fig. 7. During the compression test of one $^{238}PuO_2$ pellet at 1200°C, we continued to deform the specimen after initial fracture. Because the pellet was surrounded by a thin niobium container, deformation proceeded by crushing of the pseudobrittle $^{238}PuO_2$ as shown in Fig. 41. During the crushing phase of deformation, the $^{238}PuO_2$ absorbed considerable energy, as shown in the load-displacement record in Fig. 42.

Analytical description of the crushing of brittle fuel or the compaction and deformation of granular fuel is difficult. We are, however, considering several mechanical tests that would help describe the response of these types of fuels. The results of such tests would greatly aid analytical studies of fuel impact.

Describing the plastic behavior of fuel is much simpler. It can be done by specifying the yield
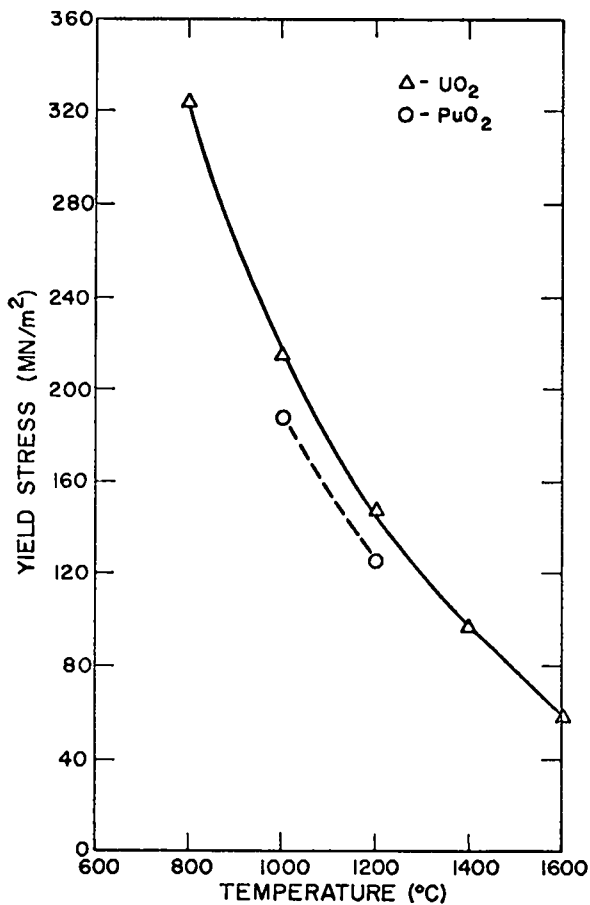
Fig. 29.

As-hot pressed plutonia-239 yield stress values vs those of UO₂. Plutonia strength levels lie below those of UO₂, but the temperature sensitivity of strength appears similar to that of UO₂.
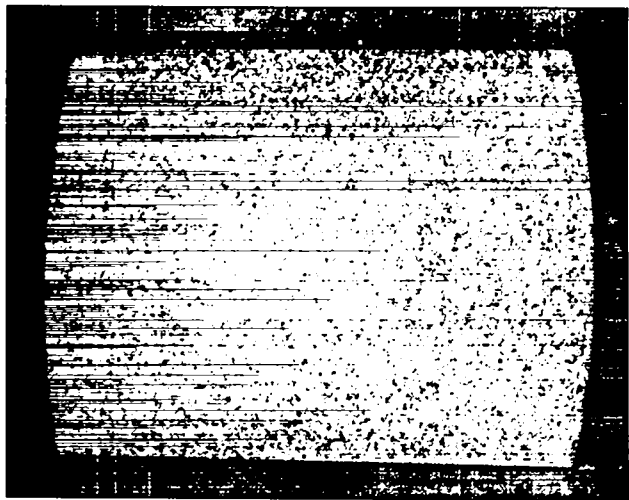
Fig. 31.

Polished cross section of HPZ-148-14, tested at 1200°C. The pellet, although it exhibited 14% strain, is still very sound, with no internal cracking evident. (8X).

Fig. 30.

Plutonia-239 specimen HPZ-148-14, tested at 1200°C, vs an untested pellet. The results of large-scale plastic deformation are obvious.

Fig. 32.

Microstructure of HPZ-148-14, tested at 120-0°C. The compression direction is vertical, and there is some suggestion that the individual granules in the pellet have become flattened in that direction. (500X).

Fig. 35.
Polished cross section of HPZ-148-15, tested at 1000°C. The large surface crack extends a significant distance into the pellet, but it is the only crack present. (8X).

Fig. 33.
Etched microstructure of HPZ-148-14, tested at 1200°C. The substoichiometric character of the material is evidenced by the two-phase mixture of $PuO_{1.52}$ (dark phase) and $PuO_{1.98}$ (light phase) present at ambient temperature. At 1200°C, however, this material was single-phase PuO_{2-x}. The two-phase structure has obscured the grain boundaries. (1000X).

Fig. 34.
Plutonia-239 specimen HPZ-148-15, after test at 1000°C. A single large axial crack has developed as a result of 16% plastic strain.

strength and the flow curve and using standard plasticity assumptions such as constancy of volume, von Mises yield criterion, and isotropic hardening. We have shown that general plastic flow in the $^{238}PuO_2$ is inhibited by internal cracks. It was observed only at very high temperature (1500°C) or in crack-free specimens like the as-hot pressed plutonia-239. The flow curves from these tests (Figs. 13, 27, and 28) are our best description of plastic flow in the fuel. Increasing the strain rate increases the yield and flow strengths appreciably and decreases the apparent ductility. It is reassuring, however, that the fuel in some impacted FSA's behaved plastically (Fig. 40) in spite of the very high strain rates (~3000/s) experienced during impact. In cooperation with LASL Group CMB-11, we are trying to solve the cracking problem and then further characterize the plastic behavior of uncracked PuO_2.

VI. CONCLUSIONS

1. The $^{238}PuO_2$ compression test pellets exhibit pseudobrittle behavior at temperatures up to
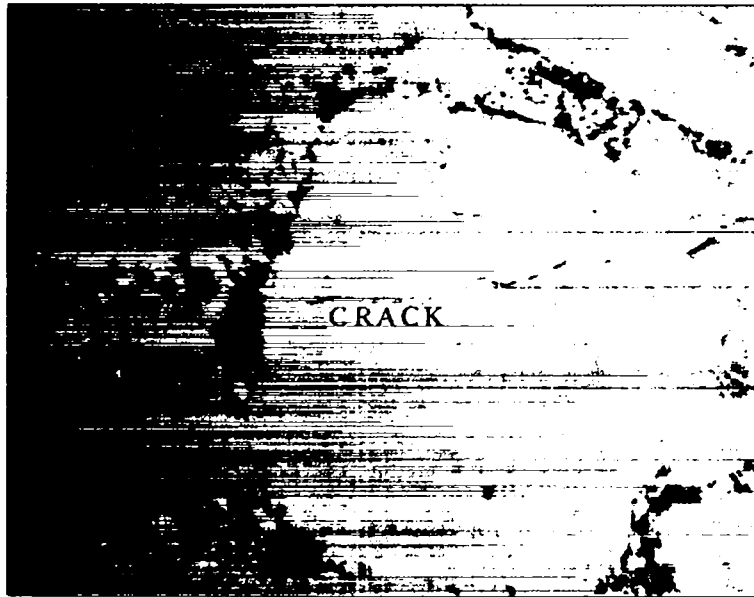
Fig. 36.
Tip of large crack (as polished, not etched) in HPZ-148-15 after test at 1000°C. (500X).

1400°C. In this temperature range, ultimate stress levels decrease with increasing storage time, decreasing density, and increasing grain size, although not markedly. Ultimate stress levels are highly sensitive to temperature and strain rate, decreasing with increasing temperature and decreasing strain rate. Generalized plastic deformation occurs at 1500°C.

2. The pseudobrittle behavior of $^{238}PuO_2$ is the result of internal cracks in the as-fabricated test specimens. Such cracks serve to "localize" plastic deformation at the crack tips, thus leading to macroscopically "brittle" behavior. The temperature and strain rate sensitivities of the ultimate stress are manifestrations of the local plastic deformation.

3. At room temperature, $^{238}PuO_2$ fractures by transgranular cleavage, whereas at elevated temperatures (1000 - 1400°C), intergranular fracture predominates.

4. $^{239}PuO_2$ fabricated by hot pressing and sintering identical to that used to fabricate $^{238}PuO_2$ developed internal cracks as a result of the sintering. As-hot-pressed plutonia-239 pellets were crack-free. The sintered specimens exhibited the pseudobrittle behavior observed in $^{238}PuO_2$ (because of the cracks),

whereas the as-hot-pressed plutonia-239 (crack-free) displayed extensive plastic deformation at temperatures as low as 1000°C.

5. Impact tests at LASL have shown that $^{238}PuO_2$ fuel in FSA's responds in either a brittle or a ductile manner. The compression properties of the cracked $^{238}PuO_2$ pellets best describe the brittle behavior. The properties of the as-hot-pressed plutonia-239 pellets are our best estimate of the plastic fuel properties.

ACKNOWLEDGMENTS

25
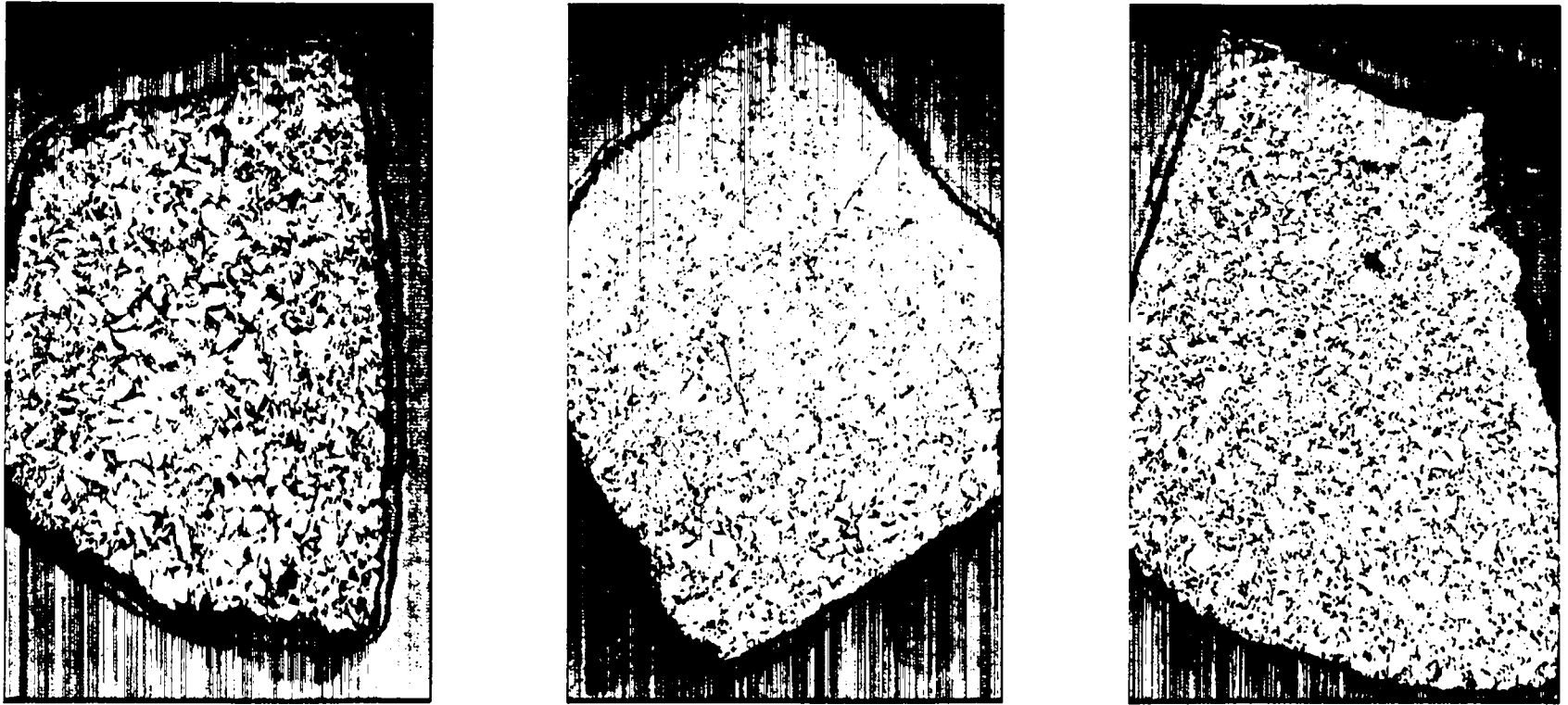
Fig. 37.
Plutonia microstructure in the polar, equatorial, and middle regions of the fuel in FSA 25.
Typically, the density of the equatorial region is greatest. (15X).
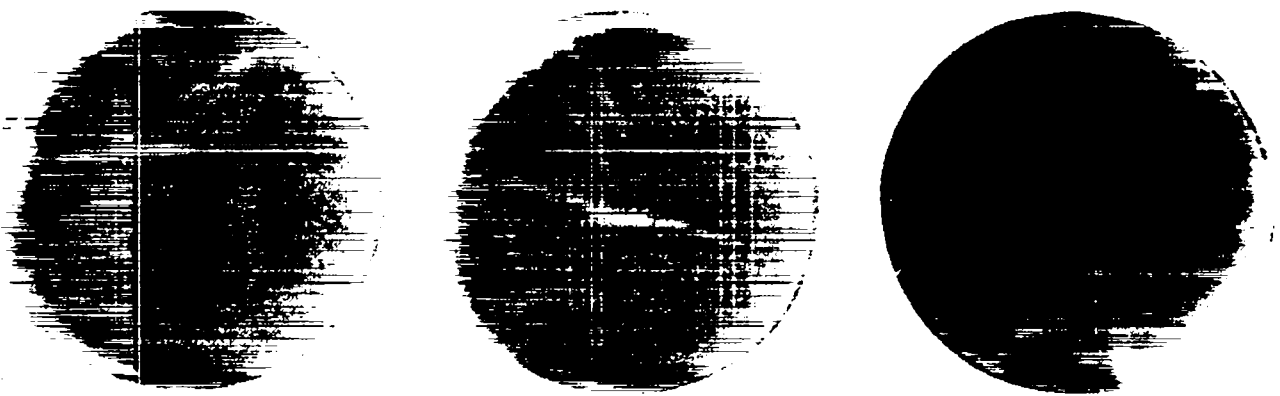
Fig. 38.
Radiographs of the fuel sphere in FSA 25 at 0, 120, and 240°. Sphere was given a short-term aging treatment at LASL.

Fig. 40.
$^{238}PuO_2$ fuel sphere after impact of FSA-33 at 86 m/s and ~370°C. Note the ductile behavior shown by the extensive shape change and imprints of the vent and iridium shell near the equator.

Fig. 39.
$^{238}PuO_2$ fuel sphere after impact of FSA 29 at 76.2 m/s and 1093°C. Note the brittle fracture behavior shown by the extensive fragmentation.

REFERENCES

1. B. A. Mueller, D. L. Rohr, and R. N. R. Mulford, "Helium Release and Microstructural Changes in $^{238}PuO_2$," Los Alamos Scientific Laboratory report LA-5524 (April 1974).

2. K. C. Radford and G. R. Terwilliger, "Compressive Deformation of Polycrystalline UO_2," J. Amer. Ceram. Soc. 58(7-8), 274-278 (1975).

Fig. 41.

Compression test specimen HPZ-390-12 tested at 1200°C in a niobium container. After initial fracture, specimen was reloaded and crushed as shown. The specimen assumes the shape of the container, although no large-scale plastic flow occured. (5X).
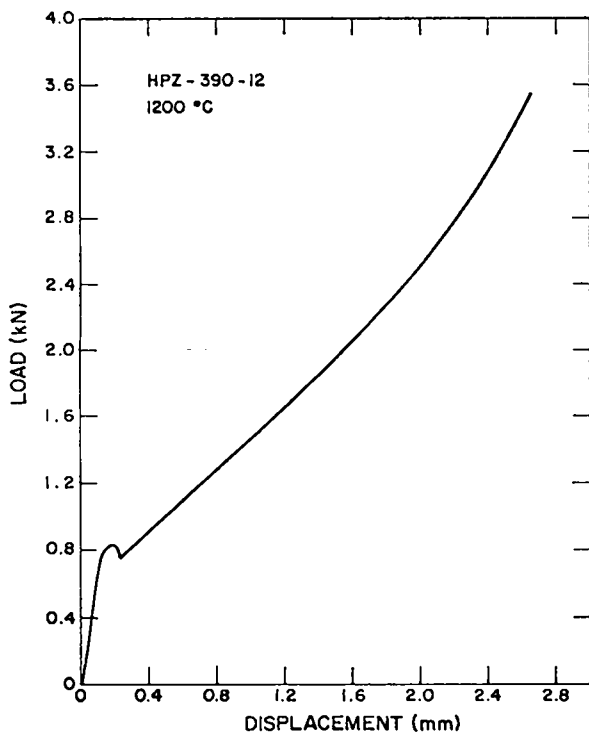
Fig. 42.

Load-displacement curve for specimen HPZ-390-12 shown in Fig. 41. Considerable energy was absorbed during crushing of the specimen after initial fracture.

3. *Engineering Properties of Selected Ceramic Materials,* J. F. Lynch, C. G. Ruderer, and W. H. Duckworth, Eds. (American Ceramic Society, Columbus, Ohio, 1966).

4. R. B. Roof, Jr., "The Effects of Self-Irradiation of the Lattice of $^{238(80\%)}PuO_2$," Los Alamos Scientific Laboratory report LA-4742 (October 1971).

5. T. D. Chikalla and R. P. Turcotte, "Self-Radiation Damage Ingrowth in $^{238}PuO_2$," Radiation Effects 19, 93-98 (1973).

6. G. L. Reynolds, B. Burton, and M. V. Speight, "Creep Fracture Processes in Uranium Dioxide," Acta. Metall. 23, 573-577 (1975).

7. R. F. Canon, J. T. A. Roberts, and R. J. Beals, "Deformation of UO_2 at High Temperatures," J. Amer. Ceram. Soc. 54, 105-112 (1971).

8. W. M. Armstrong, W. R. Irvine, and R. H. Martinson, "Creep Deformation of Stoichiometric Uranium Dioxide," J. Nucl. Mater. 7 (2), 133-141 (1962).

9. L. E. Poteat and C. S. Yust, "Creep of Polycrystalline Thorium Dioxide," J. Amer. Ceram. Soc. **49** (8), 410-414 (1966).

10. L. E. Poteat and C. S. Yust, "Grain Boundary Reactions During Deformation," in *Ceramic Microstructures, Their Analysis, Significance and Production,* R. M. Fulrath and J. A. Pask, Eds. (John Wiley & Sons, Inc., New York, 1968), pp. 646-656.

11. C. S. Yust and J. T. A. Roberts, "On the Observation of Lattice and Grain Boundary Dislocations in UO₂ Deformed at High Temperatures," J. Nucl. Mater. **48**, 317-329 (1973).

12. M. S. Seltzer, B. A. Wilcox, and A. H. Clauer, "The Influence of Stoichiometric Defects on the Creep of Oxides with the Flourite Structure," in *Defects and Transport in Oxides,* M. S. Seltzer and R. I. Jaffee, Eds. (Plenum Press, New York, 1974), pp. 443-457.

13. E. M. Cramer, "Performance of Multihundred-Watt Fueled-Sphere Assemblies in the Safety Verification Test," Los Alamos Scientific Laboratory report LA-6082 (January 1976).

14. E. M. Cramer, "Performance of Multihundred-Watt Fueled-Sphere Assemblies in the Safety Sequential Test Program," Los Alamos Scientific Laboratory report LA-5916 (July 1975).

APPENDIX A

ROOM TEMPERATURE INDENTATION FRACTURE OF PUO₂

Recent theoretical and experimental work[1-3] has suggested that basic fracture parameters of brittle materials can be deduced from measurements of cracking around microhardness indentations. Specifically, one can obtain values of the critical stress intensity factor, K_c, which is related to the fracture surface energy of the material. This term governs the stress at which a brittle material will fracture catastrophically from a given size of fracture-initiating defect. The higher the value of K_c, the higher the fracture stress for a constant fracture-initiating defect.

The microhardness indentation method for obtaining K_c is more convenient than other, more conventional, fracture mechanics methods. The other methods require relatively large specimens, but only a small, polished specimen is required for the indentation technique. This makes it ideal for ²³⁸PuO₂, large specimens of which are difficult to make and handle. Furthermore, the cracks in the present as-fabricated material pose no special problem, as they are simply avoided in making the microhardness indentations. The indentation fracture technique is potentially adaptable to elevated temperatures. Its major disadvantage is that, at its present stage of development, it can give only approximate K_c values.

Figure A-1 shows a 300-g diamond pyramid microhardness indentation in ²³⁸PuO₂. Sharp cracks emanate from the corners of the microhardness indentation. Actually, these cracks extend a considerable distance below the indentation itself, and they approximate semicircular surface flaws. By measuring the crack length and indentation dimensions at a given microhardness load, one can calculate the critical stress intensity factor[1]

$$K_c = \frac{(1-2\nu)\,P}{2^{1/2}\,\pi^{5/2}\,Z_0\,C^{1/2}} \quad,$$

where ν is Poisson's ratio, P is the microhardness load, Z_0 is the plastic deformation depth, and C is the crack depth below the indentation. The principal assumption is that the cracks produced by the indentation are semicircular, so the crack depth can
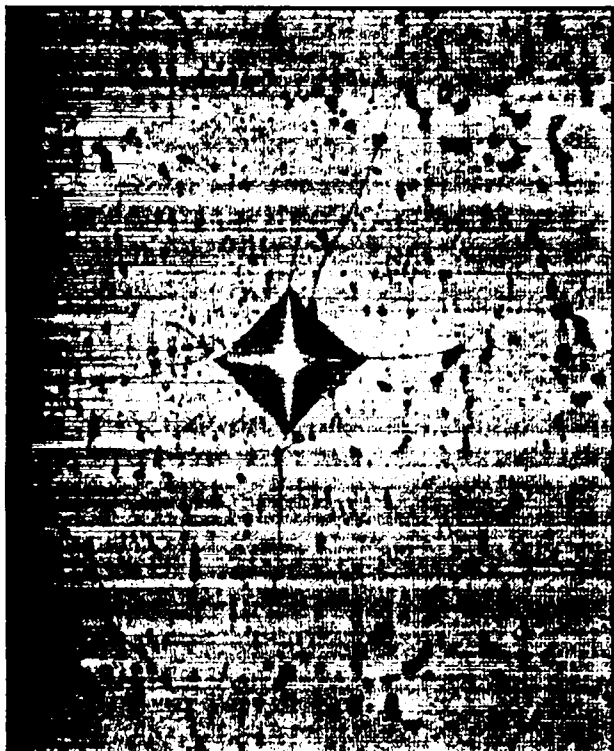
Fig. A-1.

A 300-g diamond pyramid indentation in a polished specimen of $^{238}PuO_2$ (Lot HPZ-116). (800X).

Fig. A-2.

A 300-g Knoop indentation in a polished specimen of $^{238}PuO_2$ (Lot HPZ-116). Very fine cracks eminate from both narrow corners of the indentation. (800X).

be deduced from measurements of the surface crack length. This has been shown to be a good approximation in other ceramics[4,5].

The indentation technique may be applied to either diamond pyramid or Knoop indentations. Figure A-2 shows a 300-g Knoop indentation in $^{238}PuO_2$. In this case, only one crack emanates from the indentation's long diagonal.

Figure A-3 shows K_c values derived using the indentation technique, as a function of microhardness load. These values should remain constant with microhardness load according to theory.[1] The open data points are from Knoop indentation experiments; the solid ones, from diamond pyramid experiments. Five different materials have been examined to date. HPZ-116 and HPZ-61 are $^{238}PuO_2$ stored for different times. CPZ is cold pressed and sintered $^{238}PuO_2$. UO_2 and $^{239}PuO_2$ (HPZ-148) have also been examined.

As shown in Fig. A-3, there are no marked differences in K_c because of the various material condi-

tions. All the K_c values lie between 0.4 and 0.9 $MN/m^{3/2}$. Thus, in terms of room temperature (actually, 30 - 40°C) fracture behavior, there seems to be little difference among $^{238}PuO_2$, $^{239}PuO_2$, and UO_2. Also, storage time has little effect on $^{238}PuO_2$. Unfortunately, we cannot compare these K_c values to conventional fracture mechanics data, as there are no such data on PuO_2 or UO_2. However, to indicate how low the PuO_2 K_c values are, hot-pressed Si_3N_4, the strongest current ceramic material whose room temperature bend strengths exceed 690 MN/m_2, has a room temperature K_c value[4] of 4.7 $MN/m^{3/2}$.

One may use these K_c values to estimate the room temperature tensile fracture stress of PuO_2, using the well-known Griffith equation for brittle fracture.[6] The Griffith equation is

$$\sigma_f = \frac{K_c}{(\pi C)^{1/2}} ,$$
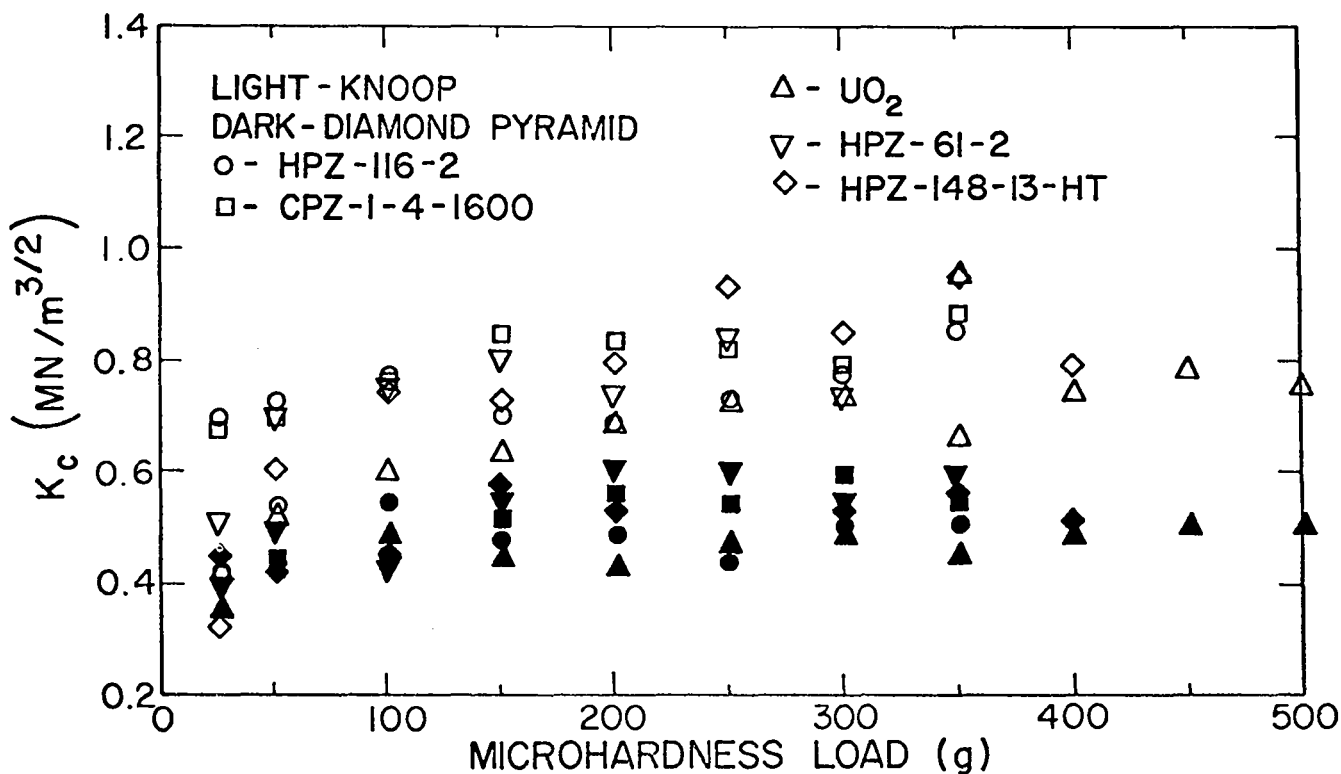
Fig. A-3.

Critical stress intensity factor, Kc, vs microhardness load, for various materials.

where C is the size of the fracture-initiating defect. Using PuO_2 K_c values of 0.4-0.9 $MN/m^{3/2}$ and a C value of 15 μm (approximately the PuO_2 grain size), we calculate the room temperature tensile fracture stress range of PuO_2 to be 58-130 MN/m^2. These fracture stresses would be lower if larger features, such as the granule size, initiated fracture in the PuO_2. We will run tests to estimate PuO_2 tensile fracture stress experimentally in the near future.

REFERENCES

1. B. R. Lawn and M. V. Swain, "Microfracture Beneath Point Indentations in Brittle Solids," J. Mat. Sci. 10, 113-122 (1975).

2. B. Lawn and R. Wilshaw, "Indentation Fracture: Principles and Applications," J. Mat. Sci. 10, 1049-1081 (1975).

3. B. R. Lawn and E. R. Fuller, "Equilibrium Penny-Like Cracks in Indentation Fracture," J. Mat. Sci. 10, 2016-2024 (1975).

4. J. J. Petrovic, L. A. Jacobson, P. K. Talty, and A. K. Vasudevan, "Controlled Surface Flaws in Hot-Pressed Si_3N_4," J. Amer. Ceram. Soc. 58 (3-4), 113-116 (1975).

5. J. J. Petrovic and L. A. Jacobson, "Controlled Surface Flaws in Hot-Pressed SiC," J. Amer. Ceram. Soc. 59 (1-2), 34-37 (1976).

6. A. A. Griffith, "The Phenomena of Rupture and Flow in Solids," Phil. Trans. Roy. Soc. Lond. A221, 163 (1920).

APPENDIX B

^{238}PUO$_2$ METALLOGRAPHY

Extensive metallography of ^{238}PuO$_2$ was performed in conjunction with its mechanical testing. General conclusions from these observations are presented here.

Large internal cracks were observed in as-fabricated pellets of Lots HPZ-61, -115, and -116 (Lots HPZ-390 and -125 were not examined for internal cracking). Figs. B-1 through B-3 show examples of such cracking. The internal cracking appeared to be a mixture of transgranular and intergranular fracturing, although we do not know which fracture mode was predominant, or at what temperature during the fabrication the cracking occured. The fact that internal cracks were observed in three different as-fabricated materal lots indicates that such cracking was general in most ^{238}PuO$_2$ test pellets, not simply an isolated effect.

The inhomogeneous porosity distribution in the microstructures of the as-fabricated higher density ^{238}PuO$_2$ materials is also indicated in Figs. B-1 through B-3. Relatively dense granules are separated by regions of high porosity. The porosity of as-fabricated low density Lot HPZ-390, Fig. B-4, seemed somewhat more uniform than that of the higher density materials. In the as-fabricated material, there were internal grain porosity, triple-point porosity, and some porosity along grain boundaries, as shown in Figs. B-5 through B-9. Twins were observed in Lot HPZ-125, Fig. B-8, but not in the other as-fabricated materials. The reason for their appearance in Lot HPZ-125 is unknown. The extensive porosity in Lot HPZ-390 is evident in Fig. B-9.

Ambient temperature fracturing of ^{238}PuO$_2$ was totally transgranular, regardless of grain size or storage time (the ambient temperature fracturing of low density Lot HPZ-390 was not examined metallographically). Figures B-10 through B-13 show examples of this fracture mode. In all cases, cracks traversed grains and grain boundaries. Figure B-13 shows transgranular fracturing of twins in Lot HPZ-125.
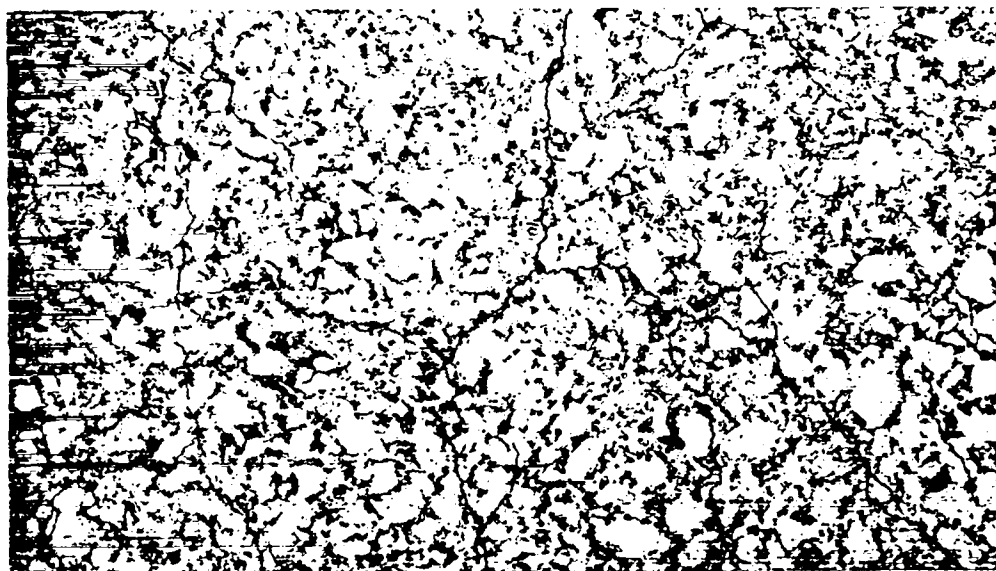
Fig. B-1.
As-fabricated HPZ-61 (90.7% theoretical density, 12-μm grains). Note extensive internal crack network and inhomogeneous microstructure. (50X).
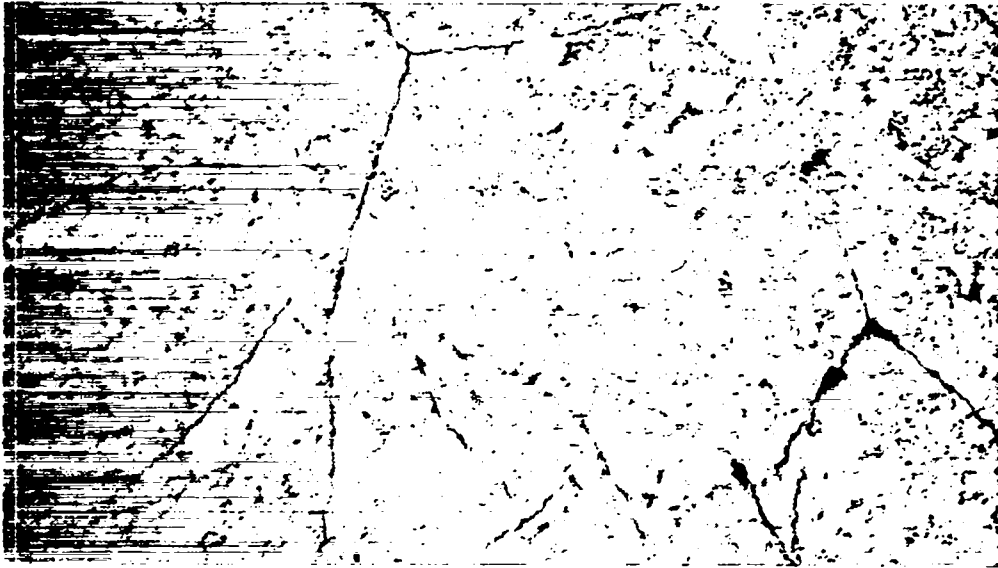
Fig. B-2.
As-fabricated HPZ-115 (92.3% theoretical density, 16-μm grains). Note extensive internal crack network and inhomogeneous microstructure. (50X).
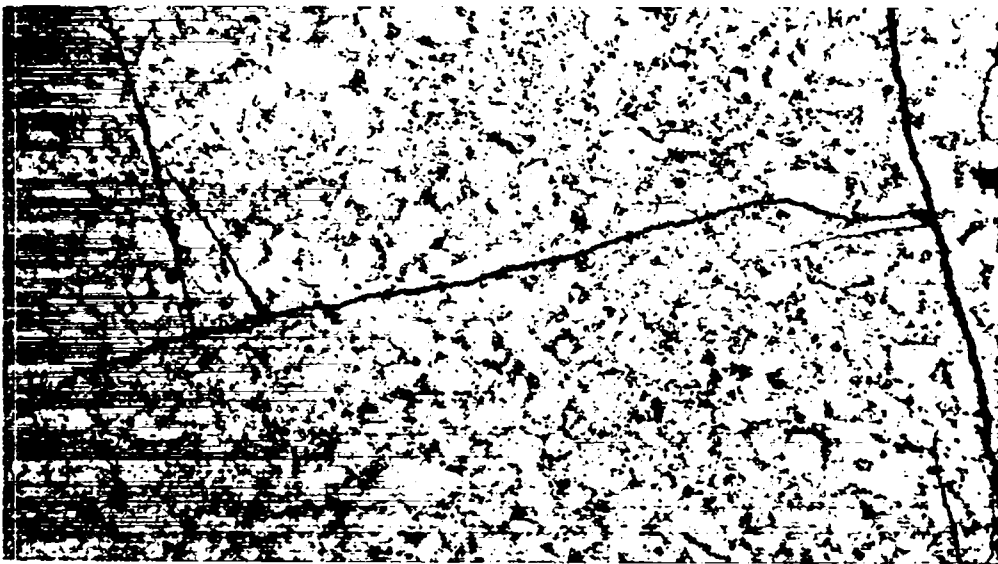
Fig. B-3.
As-fabricated HPZ-116 (92.1% theoretical density, 12-μm grains). Note extensive internal crack network and inhomogeneous microstructure. (60X).
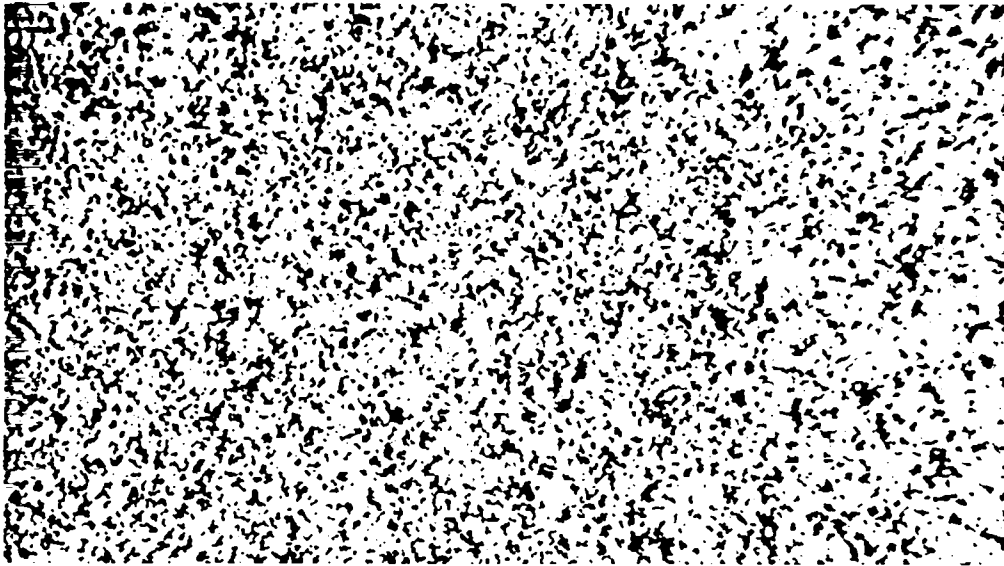
Fig. B-4.

As-fabricated HPZ-390 (78-79% theoretical density, 12-μm grains). The microstructure is more homogeneous than that of the higher density material. (100X).
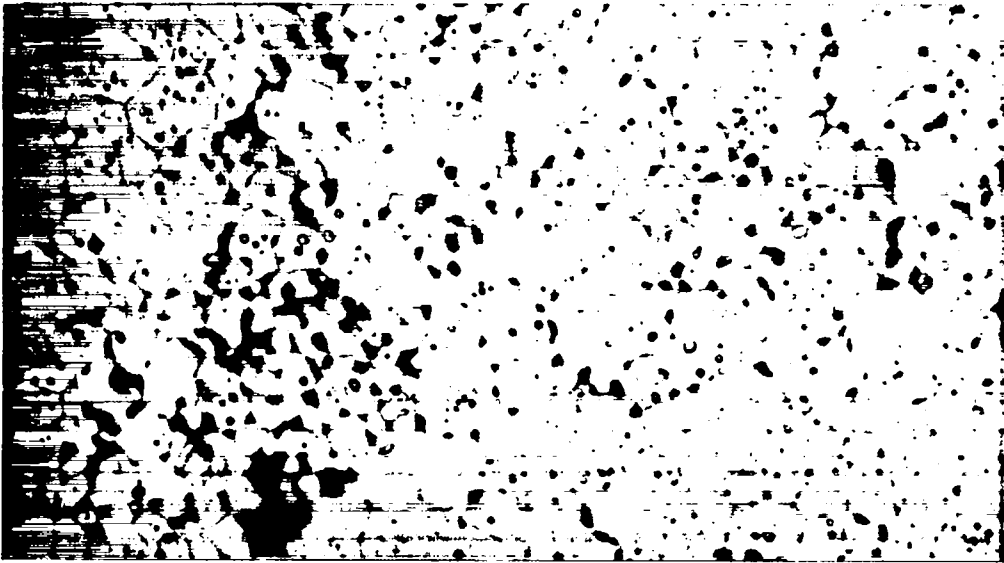
Fig. B-5.

Specimen HPZ-61-1, tested at ambient temperature after 505-day ambient temperature storage. Note internal grain porosity and grain boundary porosity. (1000X).
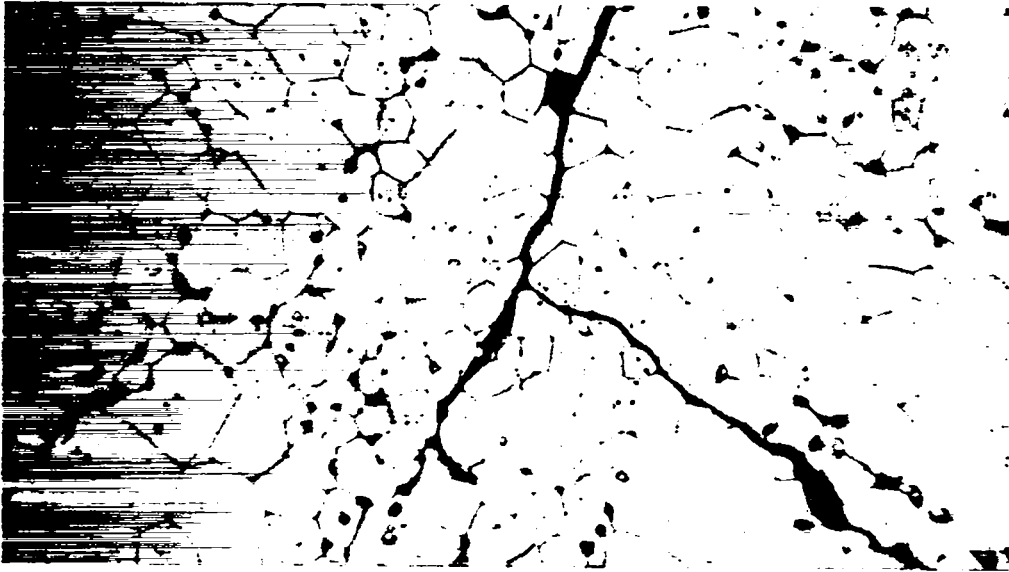
Fig. B-6.
Microstructure of as-fabricated HPZ-115 specimen. Note internal grain porosity and grain boundary porosity. (500X).
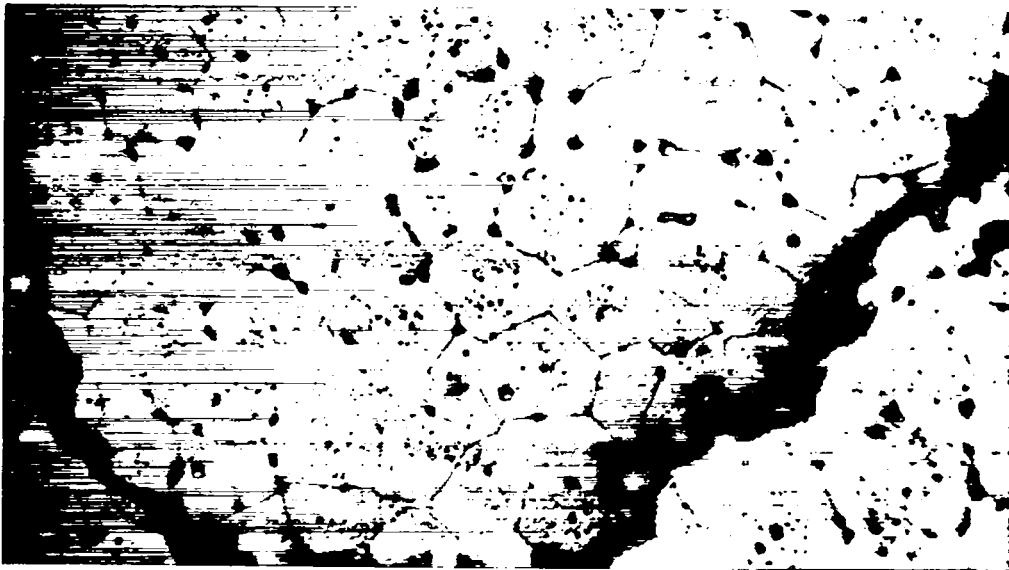
Fig. B-7.
Microstructure of as-fabricated HPZ-116 specimen. Note internal grain porosity and grain boundary porosity. (1000X).

Fig. B-8.

Microstructure of as-fabricated HPZ-125 (91% theoretical density, 10-μm grains). Note internal grain porosity, grain boundary porosity, and presence of twins. (1500X).
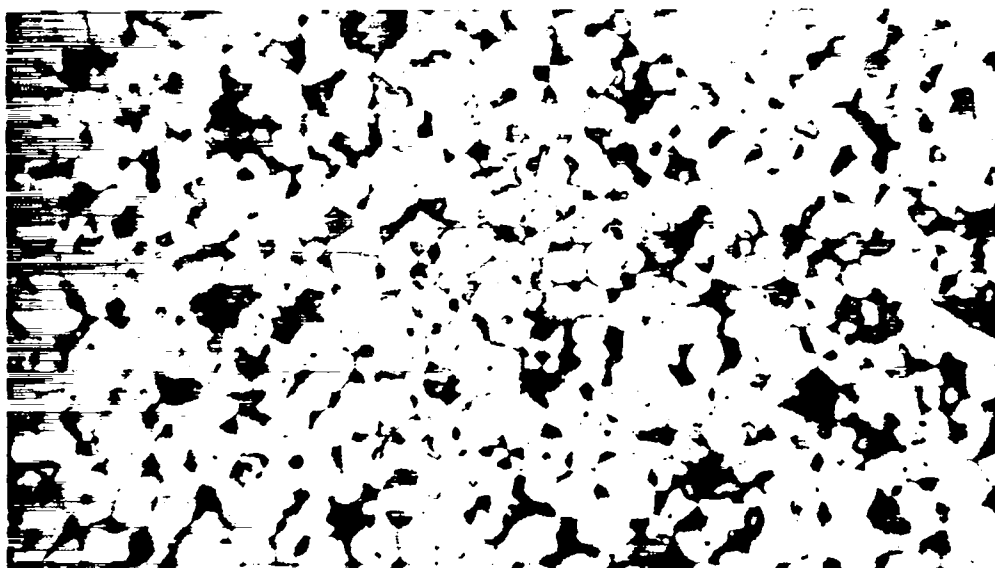
Fig. B-9.

Microstructure of as-fabricated HPZ-390, showing internal grain porosity and extensive grain boundary porosity. (500X).
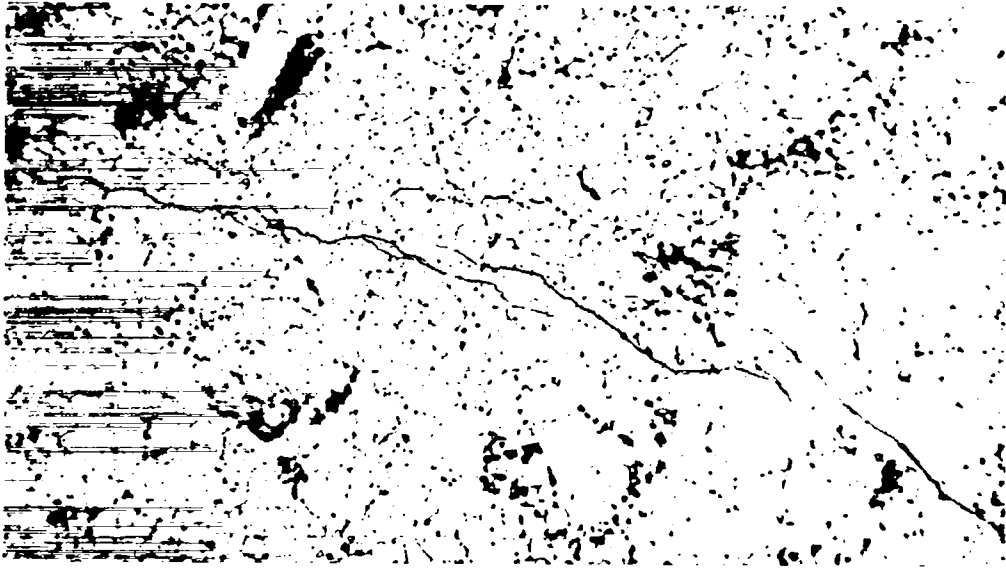
Fig. B-10.
Specimen HPZ-61-1, tested at ambient temperature after 505-day ambient temperature storage. Note transgranular fracture mode. (500X).
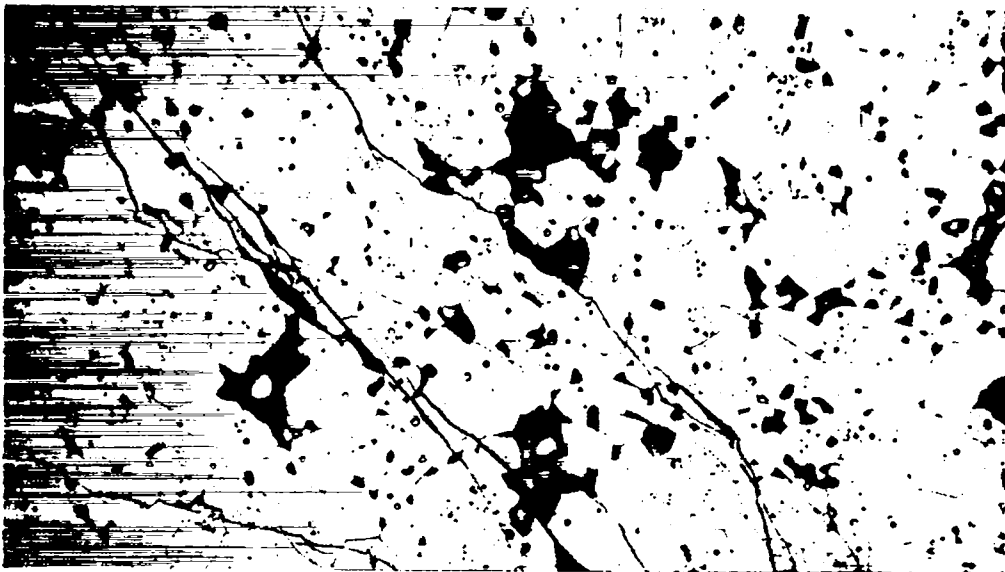
Fig. B-11.
Specimen HPZ-115-3, tested at ambient temperature after 176-day ambient temperature storage. Note transgranular fracturing. (500X).
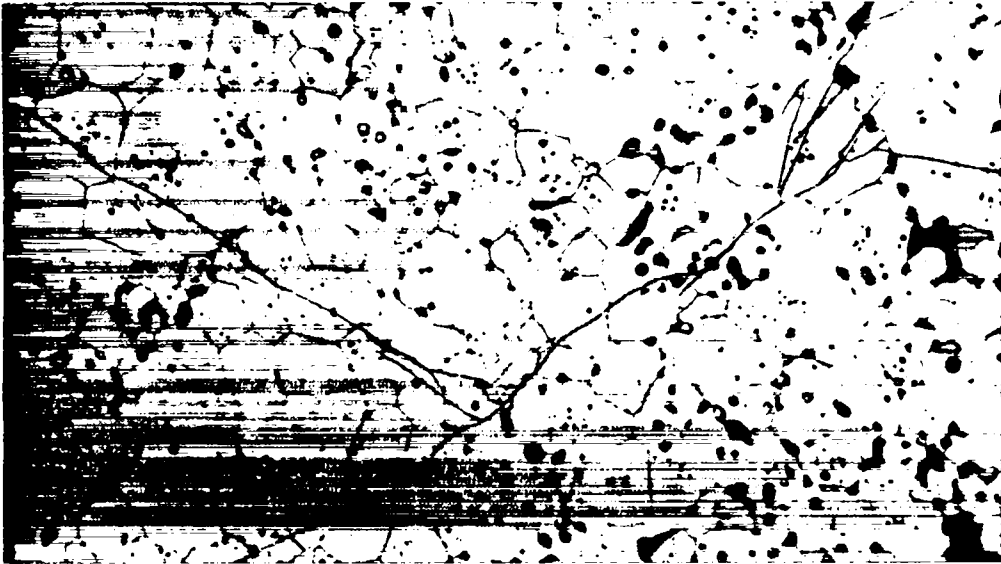
Fig. B-12.

Specimen HPZ-116-9, tested at ambient temperature after 181-day ambient temperature storage. Fracturing is transgranular. (500X).
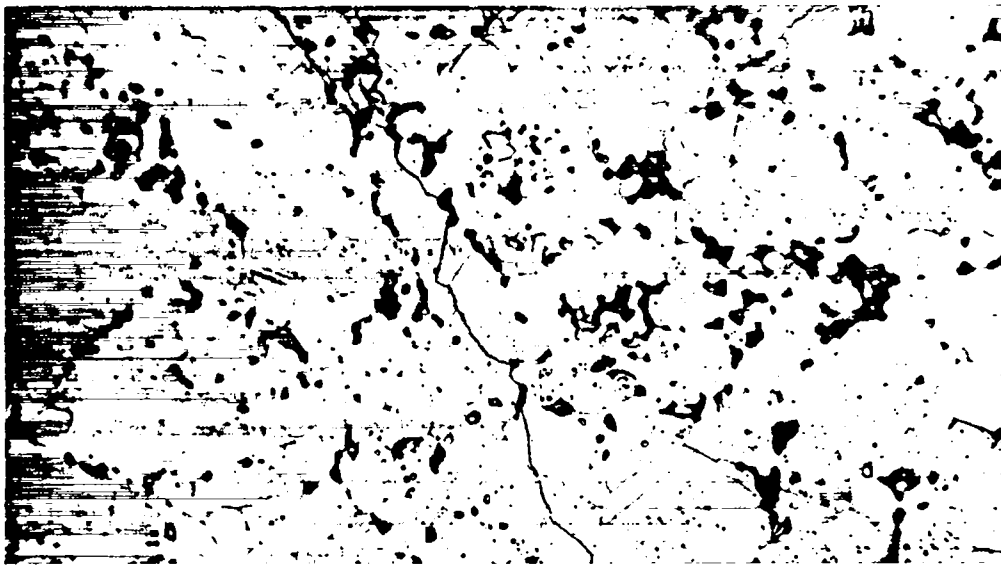
Fig. B-13.

Specimen HPZ-125-4, tested at ambient temperature after 2-day ambient temperature storage, ≤45-min exposure to 1400°C, and 82 days further storage at ambient temperature. Fracture traverses both grains and twins. (500X).

38

At elevated temperatures $^{238}PuO_2$ fractured intergranularly. At 1000°C, fracturing was mainly intergranular, but slight transgranular fracturing also occured. The fracture mode in various $^{238}PuO_2$ lots at 1400°C was totally intergranular in all material conditions, as shown in Figs. B-14 through B-18. Intense areas of intergranular separations adjacent to large cracks suggested that such separations played a role
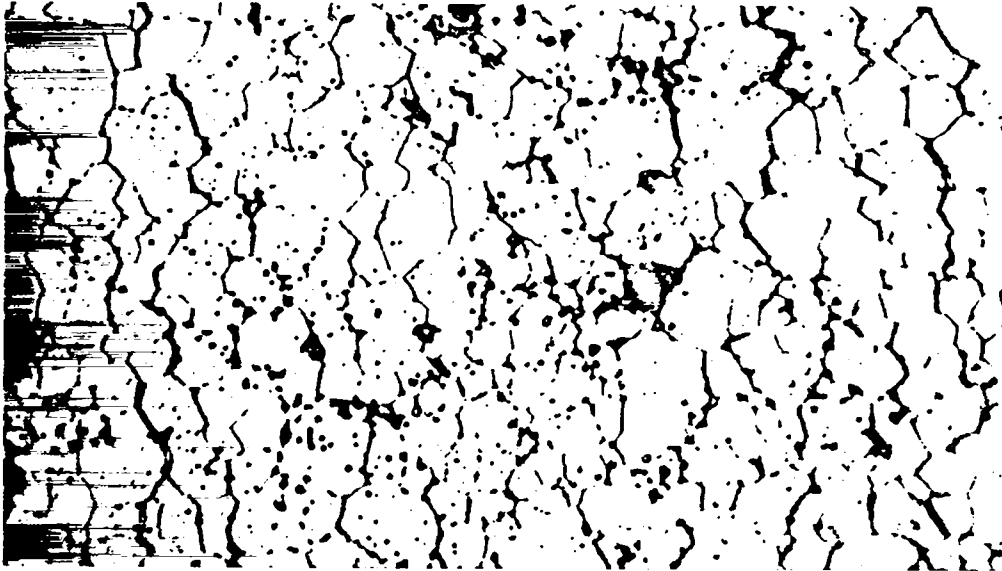
Fig. B-14.

Specimen HPZ-61-5, tested at 1400°C after 366-day ambient temperature storage. Fracture is intergranular. (500X).
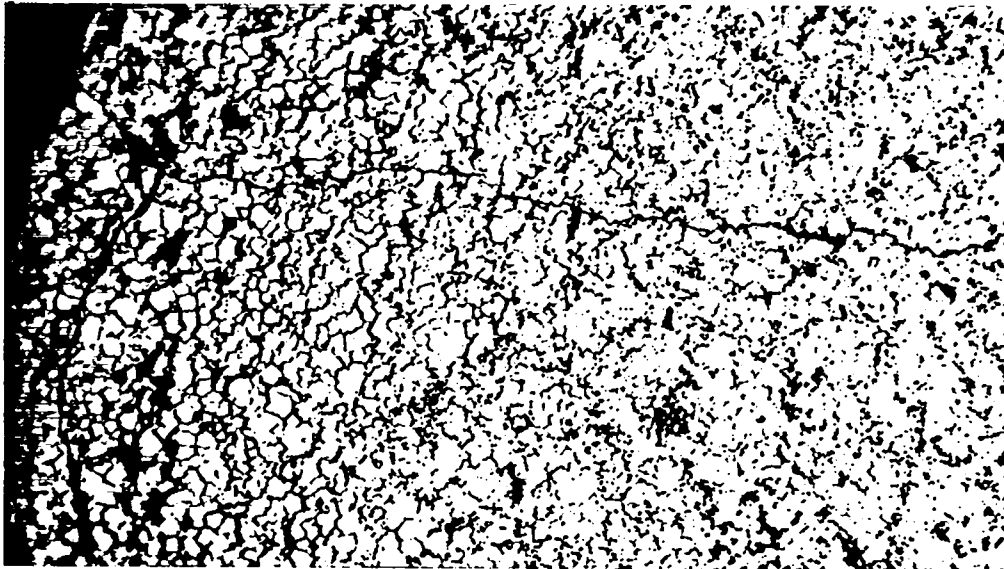
Fig. B-15.

Specimen HPZ-115-1, tested at 1400°C after 113-day ambient temperature storage. Note intense intergranular fracturing near the large crack at right. (100X).
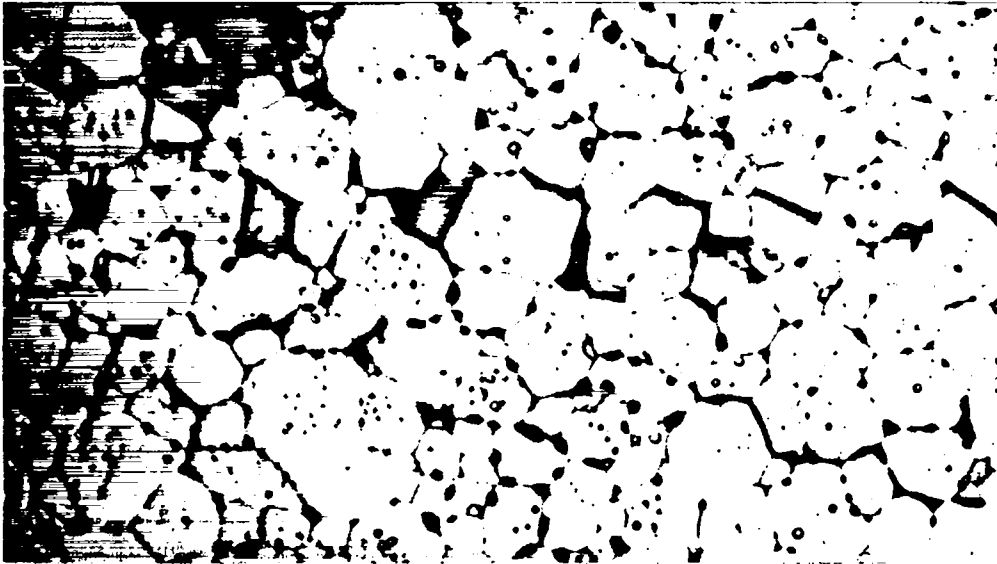
Fig. B-16.

Specimen HPZ-116-7, tested at 1400°C after 57-day ambient temperature storage. Note intergranular separations. (1000X).
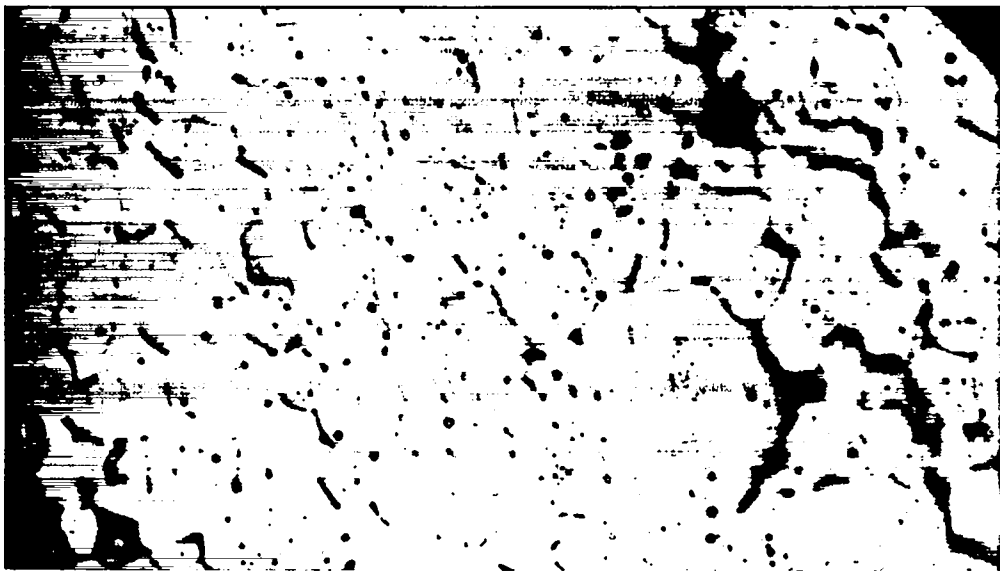
Fig. B-17.

Specimen HPZ-125-5, tested at 1400°C after 1-day ambient temperature storage. Note intergranular separations and general absence of grain boundary helium bubbles. (1000X).
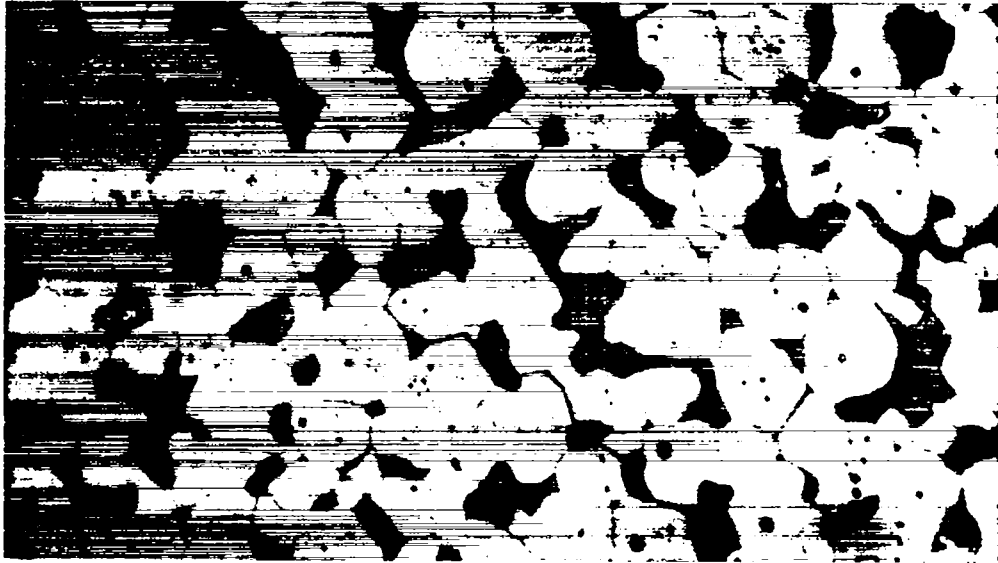
Fig. B-18.
Specimen HPZ-390-22, tested at 1400°C after 752-day ambient temperature storage. Fracturing was intergranular. No extensive grain boundary helium bubble formation has occurred. The gray material is metallographic potting resin. (1000X).

in large crack propagation, although the role of such separations in crack nucleation is unknown at present. Some of the grain edges and corners at intergranular separations were rounded instead of sharp, suggesting operation of diffusion processes after the intergranular separations had occured.

Development of grain boundary helium bubbles was also noted at elevated temperatures. Although no large-scale bubble formation was observed at 1000°C (at least not on the scale of the micrographs), obvious grain boundary helium bubble stringers were present after testing at 1400°C. Figures B-19 through B-21 show examples from Lots HPZ-61, -115, and -116. Helium bubble formation was minimal in Lot HPZ-125 at 1400°C (Fig. B-17), because this material was tested after a very short storage time. Bubble formation was also minimal at

1400°C in Lot HPZ-390 (Fig. B-18), possibly because of the material's lower density.

Macroscopic plastic deformation was observed in $^{238}PuO_2$ at 1500°C, in specimens of Lots HPZ-61, -115, and -116 (Lots HPZ-125 and -390 were not tested at this temperature). Specimens were relatively intact after testing, as shown in Figs. B-22 through B-24, in the sense that large-scale shard formation had not occured. Polished cross sections, Figs. B-25 through B-27, showed deformation occuring along 45° shear bands. This deformation was accompanied by cavitation caused by extensive areas of intergranular separations at this temperature (Figs. B-28 through B-30). Intergranular separations showed considerable rounding of grain boundary features at this temperature.
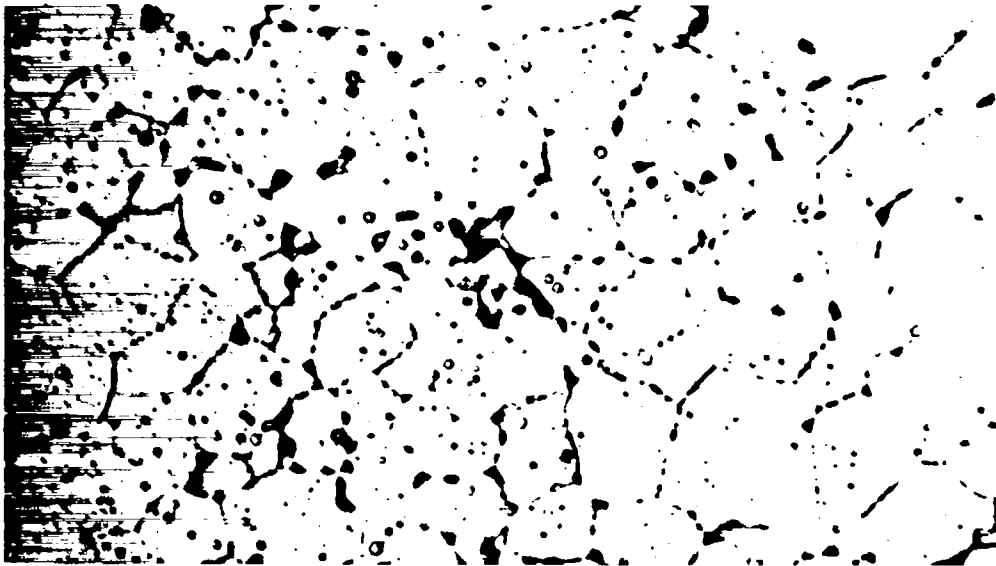
Fig. B-19.

Specimen HPZ-61-5, tested at 1400°C after 366-day ambient temperature storage. Extensive helium bubbles have formed at the grain boundaries. (1000X).
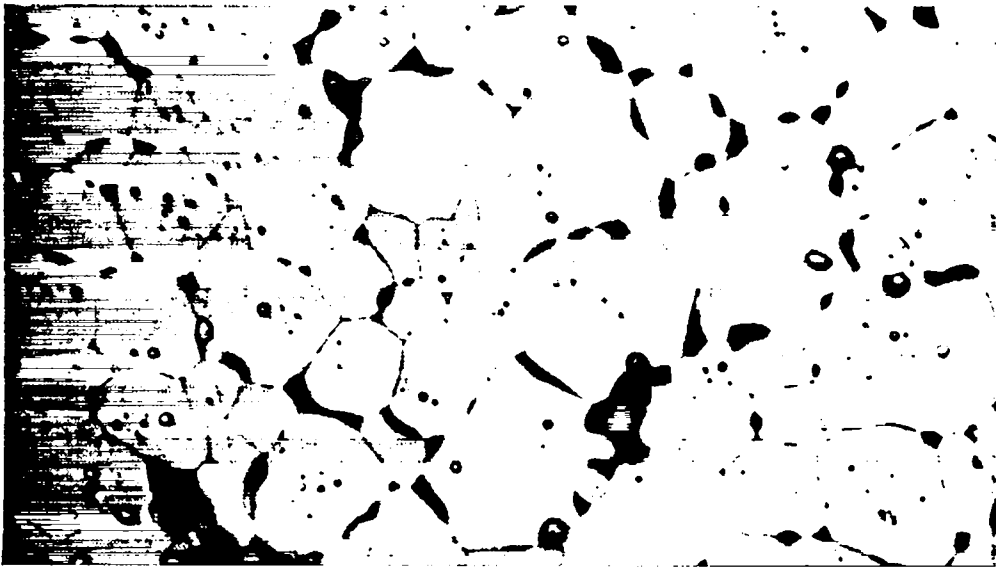

Fig. B-20.

Specimen HPZ-115-1, tested at 1400°C after 113-day ambient temperature storage. Note grain boundary helium bubble formation. (1000X).
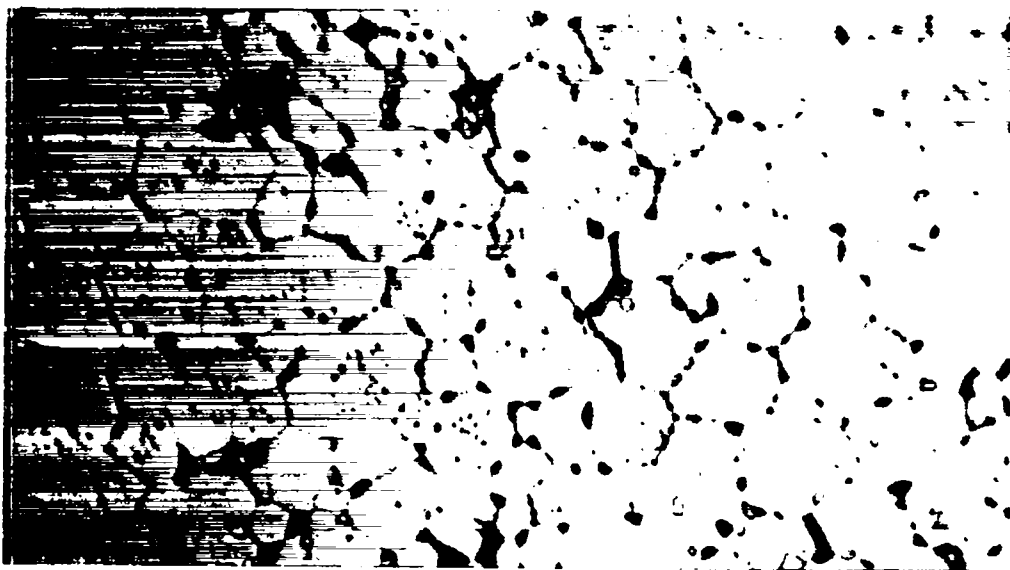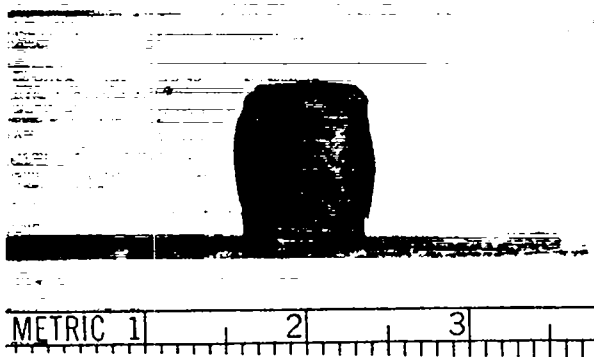
Fig. B-21.
Specimen HPZ-116-7, tested at 1400°C after 57-day ambient temperature storage. Extensive
helium bubbles have formed at the grain boundaries. (1000X).

Fig. B-22.
Specimen HPZ-61-11, tested at 1500°C after 604-day ambient temperature storage, exhibited 8.3% plastic strain and is noticeably barrelled. The granular surface layer resulted from interaction with the niobium containment can. (~2X).
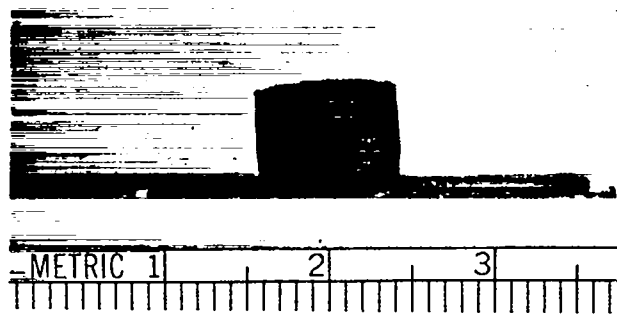
Fig. B-23.
Specimen HPZ-115-8, tested at 1500°C after 278-day ambient temperature storage, exhibited 8.5% plastic strain. Surface cracking is evident. (~2X).

43
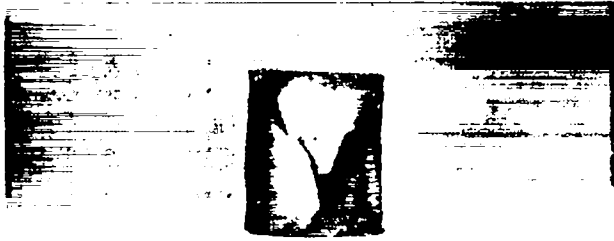
Fig. B-24.
Specimen HPZ-116-5, tested at 1500°C after 263-day ambient temperature storage, exhibited 7.6% plastic strain and shows surface chipping and cracking. (~2X).
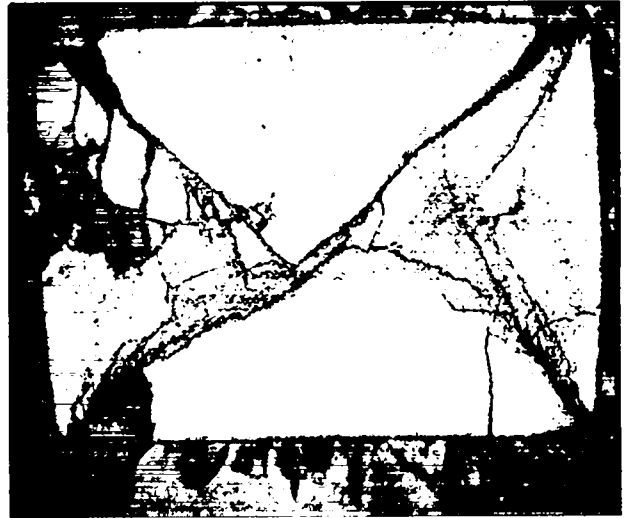
Fig. 26.
Specimen HPZ-115-8, tested at 1500°C after 278-day ambient temperature storage. The polished longitudinal cross section shows cracking, cavitation, and sliding along 45° directions. (~8X).

Fig. B-25.
Specimen HPZ-61-11, tested at 1500°C after 604-day ambient temperature storage. The polished longitudinal cross section shows extensive cracking and cavitation along 45° directions. (~6X).

Fig. B-27.
Specimen HPZ-116-5, tested at 1500°C after 263-day ambient temperature storage. The polished longitudinal cross section shows extensive cracking along 45° directions and many as-fabricated internal cracks. (~10X).
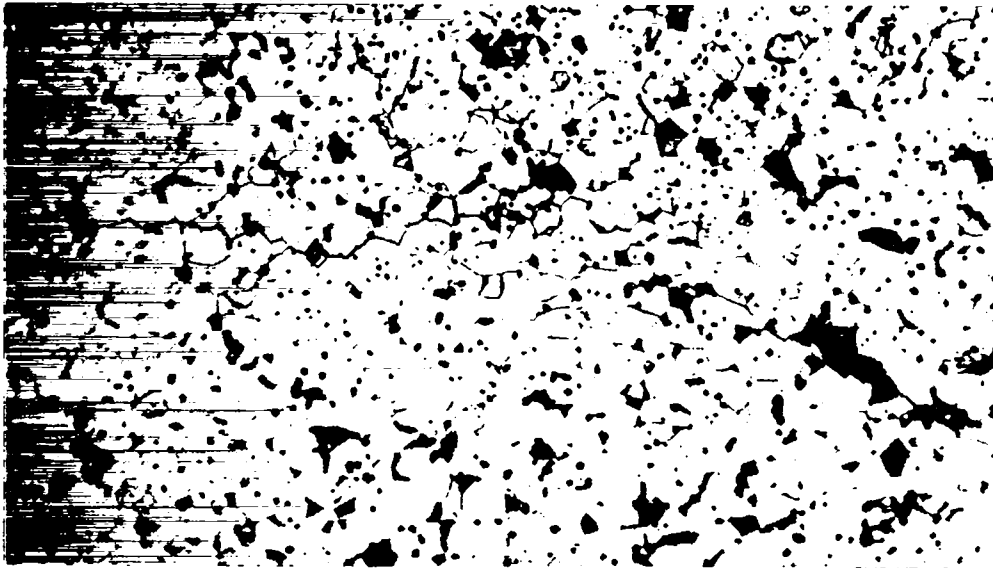
Fig. B-28.
Specimen HPZ-61-11, tested at 1500°C after 604-day ambient temperature storage. Note intergranular fracturing. (200X).

Fig. B-29.

Specimen HPZ-115-8, tested at 1500°C after 278-day ambient temperature storage. Note rounded grain boundary separations. The grain boundary material is substoichiometric plutonia. (1000X).
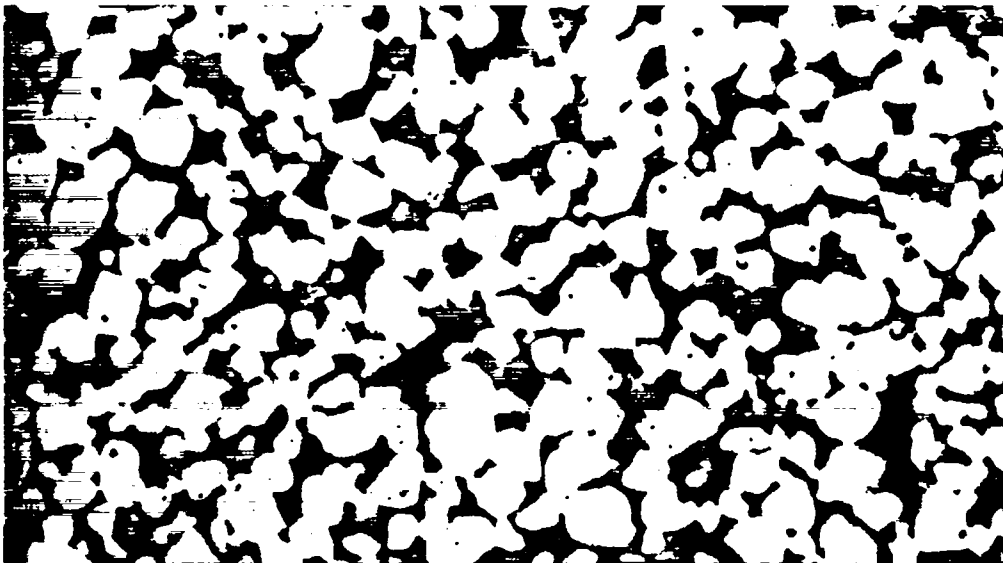
Fig. B-30.

Specimen HPZ-116-5, tested at 1500°C after 263-day ambient temperature storage. Fracturing was intergranular, as shown by extensive grain boundary separations. The grains are considerably rounded. The dark material is metallographic potting resin. (500X).

APPENDIX C

^{238}PUO$_2$ FRACTURE SURFACES

Fracture surfaces of ^{238}PuO$_2$ specimens were examined using replica electron microscopy (REM) and scanning electron microscopy (SEM), after mechanical testing. Ambient temperature ^{238}PuO$_2$ fracturing was transgranular in all the material conditions examined. Examples are shown in Figs. C-1 through C-5. Ambient temperature fracture surfaces showed distinct cleavage steps. The fracture path cut through the grains, revealing the internal grain porosity.

At elevated temperature (1000°C or higher), intergranular fracturing was observed, with evident grain and grain boundary definition (Figs. C-6 through C-13). Grain boundary helium bubbles were revealed on many of the grain faces. An interesting example of the equilibrium geometry between a

helium bubble and a ^{238}PuO$_2$ grain boundary is shown in Fig. C-7. At 1500°C, internal grain features with distinct geometrical character were noted (Fig. C-14). These features maybe related to dislocation activity in the ^{238}PuO$_2$ at 1500°C.

Areas of rounded grains, which were relatively smooth and featureless, were very prominent on the fracture surfaces of tested ^{238}PuO$_2$ specimens. (Figs C-15 through C-21). We believe that such areas represent cracked material that had been exposed to high temperatures, thus allowing diffusive processes to smooth out the features on the fracture surface. These rounded grain regions were observed in all the material conditions tested and at all test temperatures, including ambient temperature (Figs. C-16 and C-18).
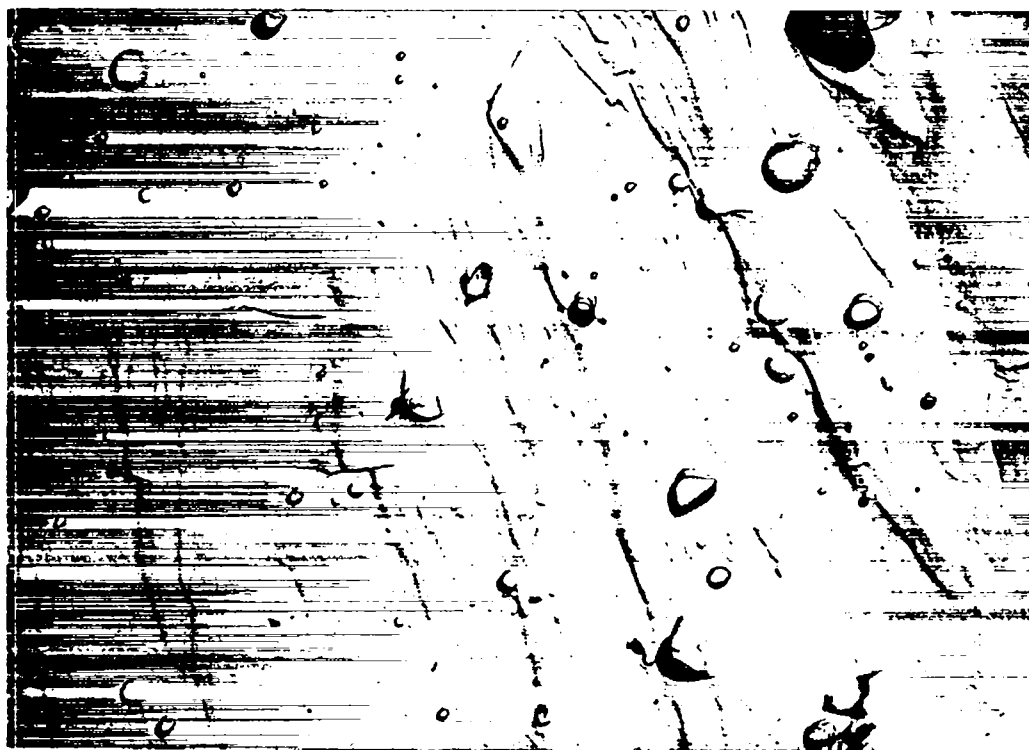

Fig. C-1.
REM of fracture surface of HPZ-61-1, tested at ambient temperature after 505-day ambient temperature storage. Note transgranular fracture mode evidenced by cleavage steps, exposure of internal grain porosity, and lack of grain boundary definition. (7000X).
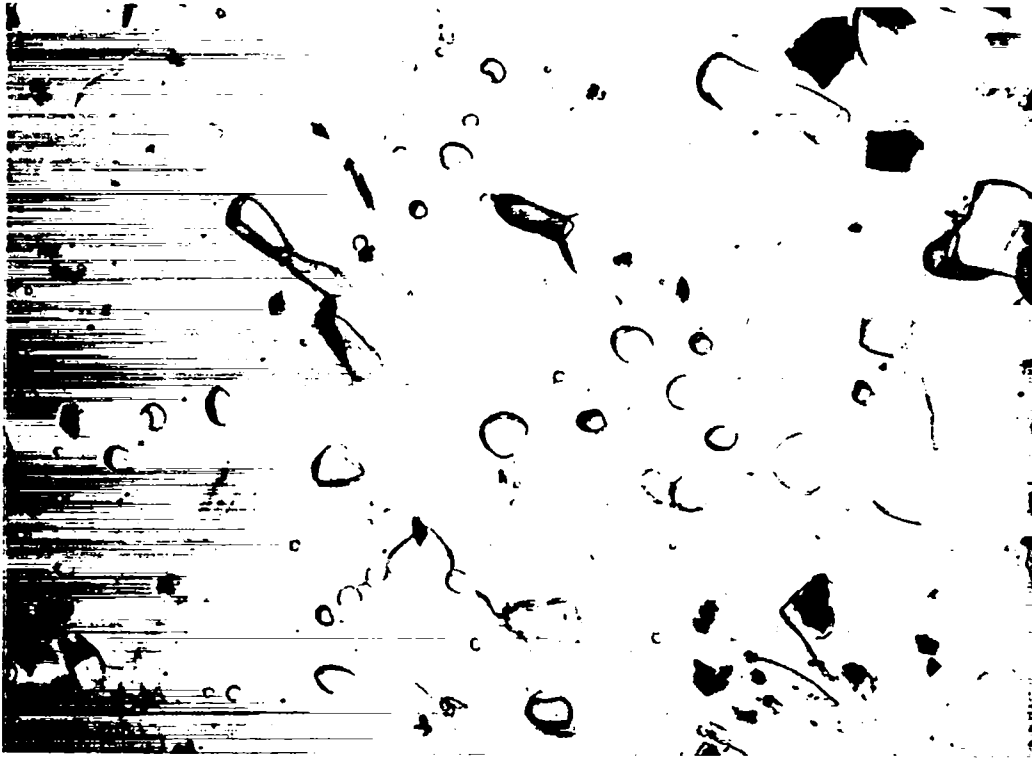
Fig. C-2.
REM of fracture surface of HPZ-115-3, tested at ambient temperature after 176-day ambient temperature storage. Note transgranular fracturing. Black particles are $^{238}PuO_2$ plucks that have adhered to the replica. (6600X).

The fact that the rounded grains were observed after ambient temperature testing is significant. The ambient temperature specimens had never been exposed to elevated temperature, except during fabrication, which suggests that these rounded grain areas were present in the as-fabricated test specimens. We believe that the rounded grain areas represent cracks in the as-fabricated test pellets, like those observed metallographically (Appendix B). The nature of these areas suggests that the cracks induced by fabrication were exposed to elevated temperature at some stage in the fabrication process, probably during sintering.

Thermal swirls (Fig. C-15) often appeared on the rounded grain surfaces. They were thought to be a thermal etching effect resulting from intersection of crystallographic planes with the edges of the rounded grains.

Fig. C-3.
REM of fracture surface of HPZ-116-12, tested at ambient temperature after 126-day ambient temperature storage. Transgranular fracturing has revealed internal grain porosity. (7000X).

Fig. C-4.
SEM of fracture surface of HPZ-116-12, tested at ambient temperature after 126-day ambient temperature storage. Note cleavage steps and internal grain porosity. (2000X).
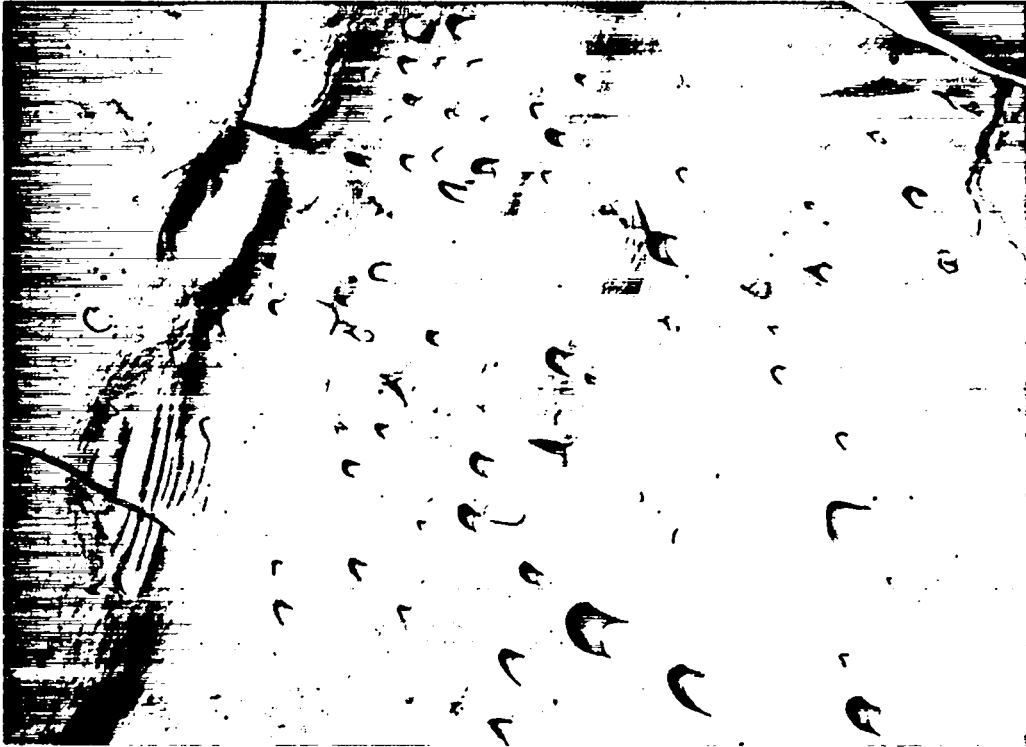
Fig. C-5.

REM of fracture surface of HPZ-125-4, tested at ambient temperature after 2-day ambient temperature storage, ≤45-min exposure to 1400°C, and 82 days further ambient temperature storage. Note transgranular fracture mode. (7000X).
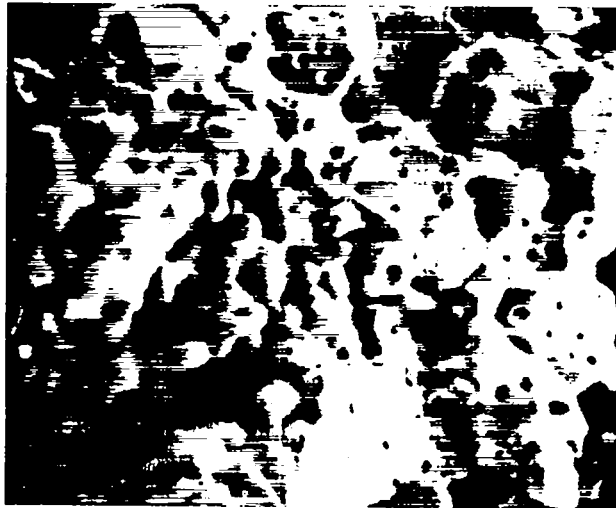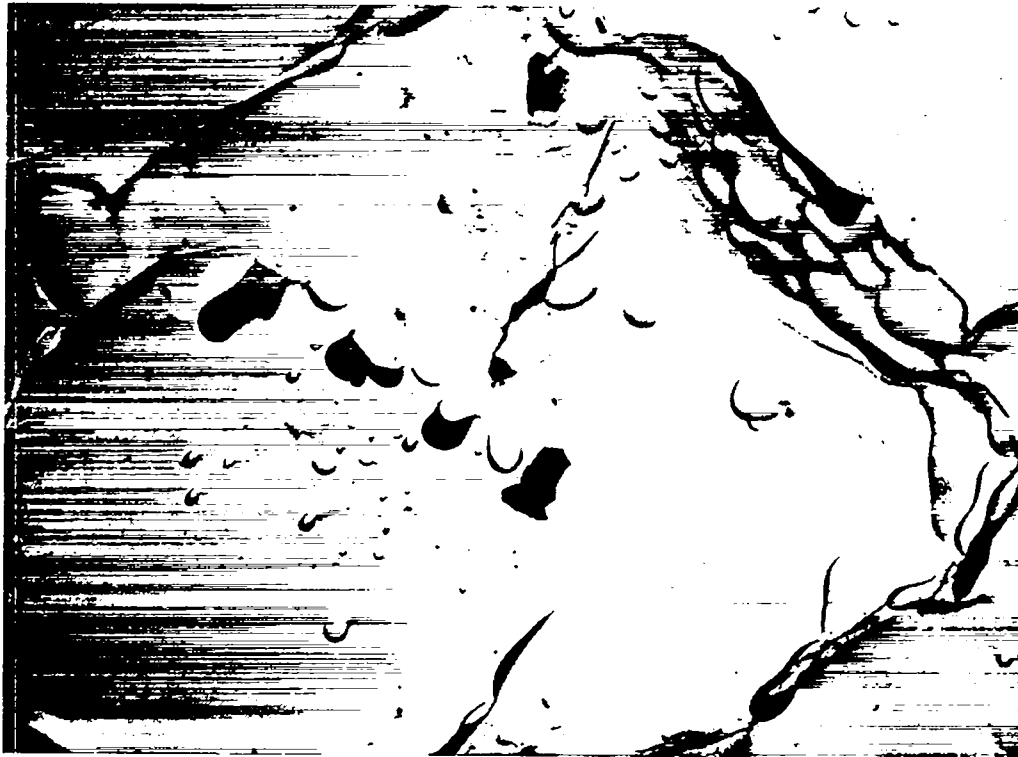

Fig. C-6.

SEM of fracture surface of HPZ-61-8, tested at 1000°C after 374-day ambient temperature storage. Intergranular fracturing has exposed grain boundary helium bubbles. (2000X).

Fig. C-7.
REM of fracture surface of HPZ-61-8, tested at 1000°C after 374-day ambient temperature storage. Note equilibrium geometry between the $^{238}PuO_2$ grain boundary and a helium bubble. (14 000X).

Fig. C-8.
SEM of fracture surface of HPZ-61-5, tested at 1400°C after 366-day ambient temperature storage. Note intergranular fracturing and globular region. (2000X).

Fig. C-9.
REM of fracture surface of HPZ-116-8, tested at 1000°C after 58-day ambient temperature storage. Fracturing is intergranular, with grain and grain boundary definition. Note grain boundary helium bubbles. (3600X).

Fig. C-10.
SEM of fracture surface of HPZ-116-8, tested at 1000°C after 58-day ambient temperature storage. Note intergranular fracture surface. (2000X).

Fig. C-11.
REM of fracture surface of HPZ-116-7, tested at 1400°C after 57-day ambient temperature storage. Note intergranular fracturing and grain boundary helium bubbles. (4600X).

Fig. C-12.
SEM of fracture surface of HPZ-116-7, tested at 1400°C after 57-day ambient temperature storage. Intergranular fracturing has exposed grain boundary helium porosity. (2000X).
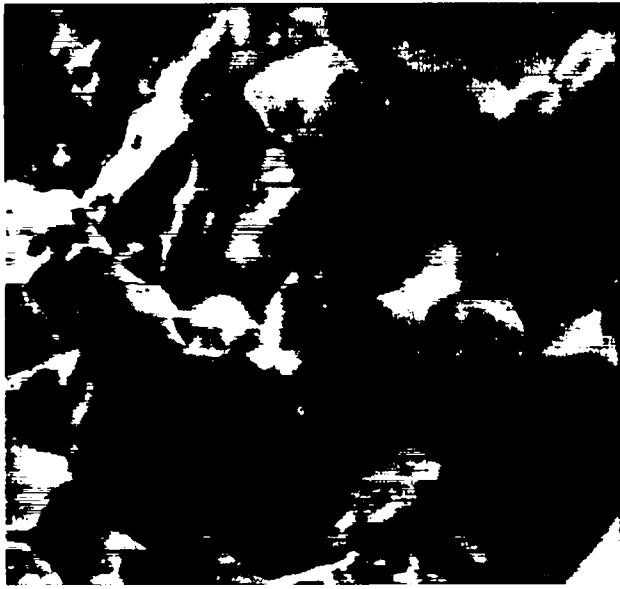
Fig. C-13.
SEM of fracture surface of HPZ-125-5, tested at 1400°C after 1-day ambient temperature storage. Note intergranular fracturing, as well as some grain boundary porosity. (2000X).

Fig. C-14.
REM of fracture surface of HPZ-61-15, tested at 1500°C after 619-day ambient temperature storage. Geometric lines may be related to dislocation activity in the $^{238}PuO_2$ at 1500°C. (4000X).
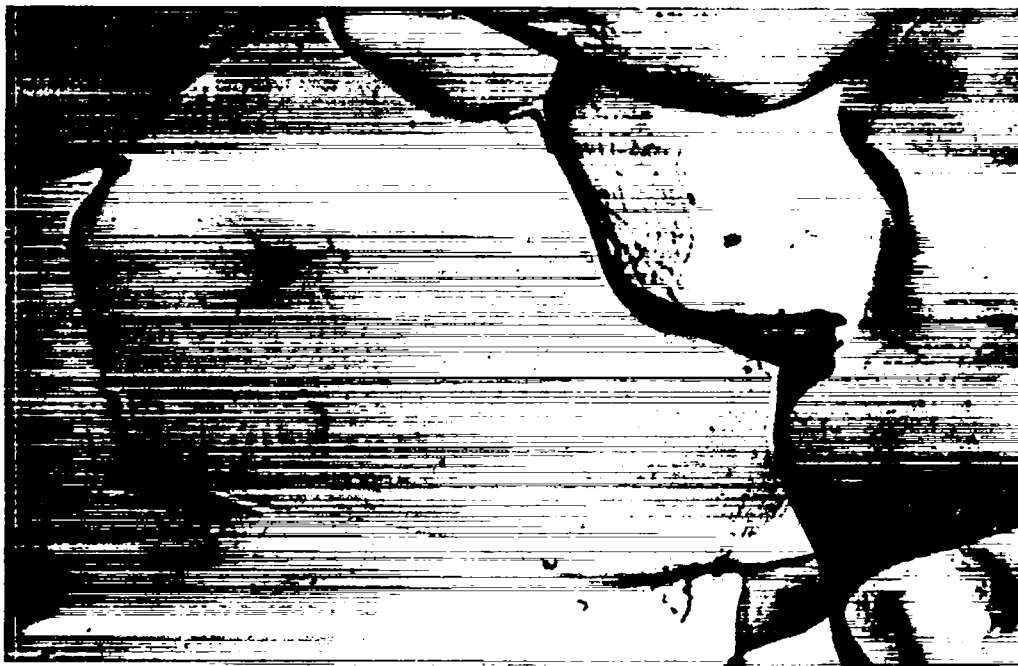
Fig. C-15.

REM of fracture surface of HPZ-61-5, tested at 1400°C after 366-day ambient temperature storage. Note rounded grains in the fracture surface. Thermal swirls are prominent on the rounded grains. (11 600X).
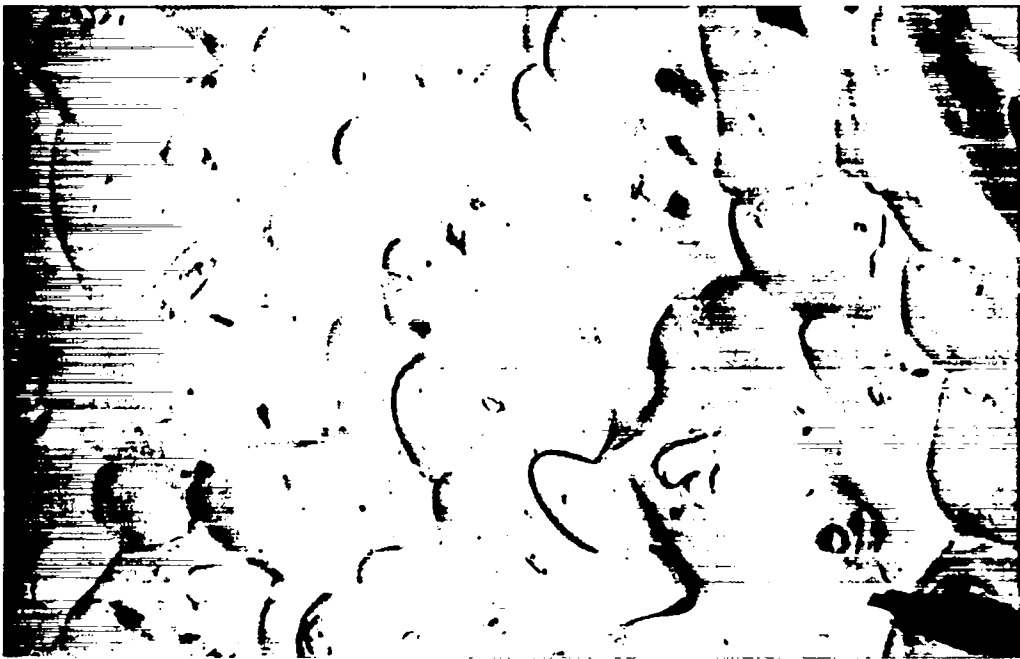

Fig. C-16.

REM of fracture surface of HPZ-115-3, tested at ambient temperature after 176-day ambient temperature storage. The fracture surface shows rounded grains even after ambient temperature testing, so the rounded grain areas were probably present in the as-fabricated test specimens. (6400X).

Fig. C-17.
REM of fracture surface of HPZ-115-1, tested at 1400°C after 113-day ambient temperature
storage. Note the smooth, featureless rounded grains. (4400X).

Fig. C-18.
REM of fracture surface of HPZ-116-12, tested at ambient temperature after 126-day am-
bient temperature storage. Note rounded grains. (7600X).

Fig. C-19.

REM of fracture surface of HPZ-116-1, tested at 1400°C after 146-day ambient temperature storage. Note rounded grains. (6800X).
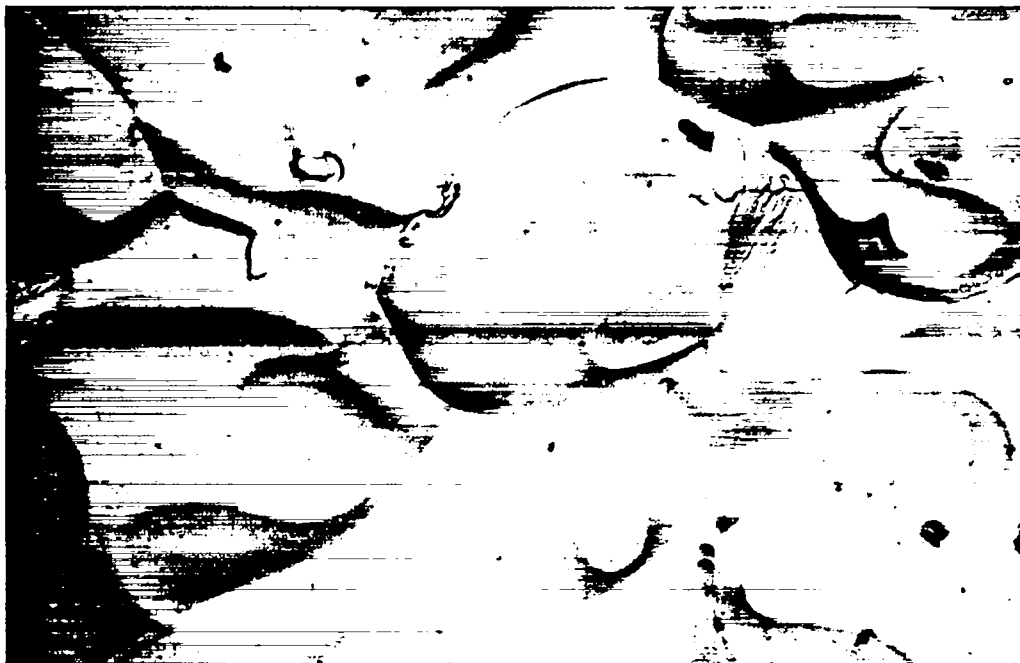

Fig. C-20.

REM of fracture surface of HPZ-125-5, tested at 1400°C after 1-day ambient temperature storage. Note rounded grains and contouring. (5400X).

Fig. C-21.
REM of fracture surface of HPZ-390-17, tested at 1400°C after 619-day ambient temperature storage. Note rounded grains. Contoured areas may represent regions of previous grain contact. (5000X).

APPENDIX D

EFFECT OF 1800°C EXPOSURE ON ^{238}PUO$_2$ MICROSTRUCTURE

To be safe, heat sources for space nuclear power systems must be able to survive a thermal ramp at very high temperatures. Therefore, the effects of such elevated-temperature exposure on the fuel material are of interest.

An as-fabricated specimen (HPZ-115-12) was annealed for 1 h at 1800°C in vacuum. This specimen had a large circumferential surface crack as-fabricated, and the annealing was done to determine whether the very high temperature exposure would heal the crack by enhanced diffusion.

Figure D-1 shows a polished cross section of the pellet after the high-temperature annealing. The internal crack network present in the as-fabricated pellet is still present, but Figs. D-2 and D-3 indicate that some crack healing may have occurred. The

tips of some of the cracks have closed up, leaving strings of separated porosity.

Figure D-4 shows crack healing that has produced a region of elongated porosity. A small segment of grain boundary apparently has been formed in this region.

An obvious effect of the elevated temperature exposure was the appearance of lath-like features (Figs. D-4 and D-5). These features are seen cutting across the grains in Fig. D-5. They are a manifestation of departure from stoichiometry at the elevated temperature, which results in a two-phase structure at room temperature. The grain boundaries are relatively free of grain boundary helium bubble stringers. Grain growth as a result of the elevated temperature exposure has not been dramatic.

Fig. D-1.
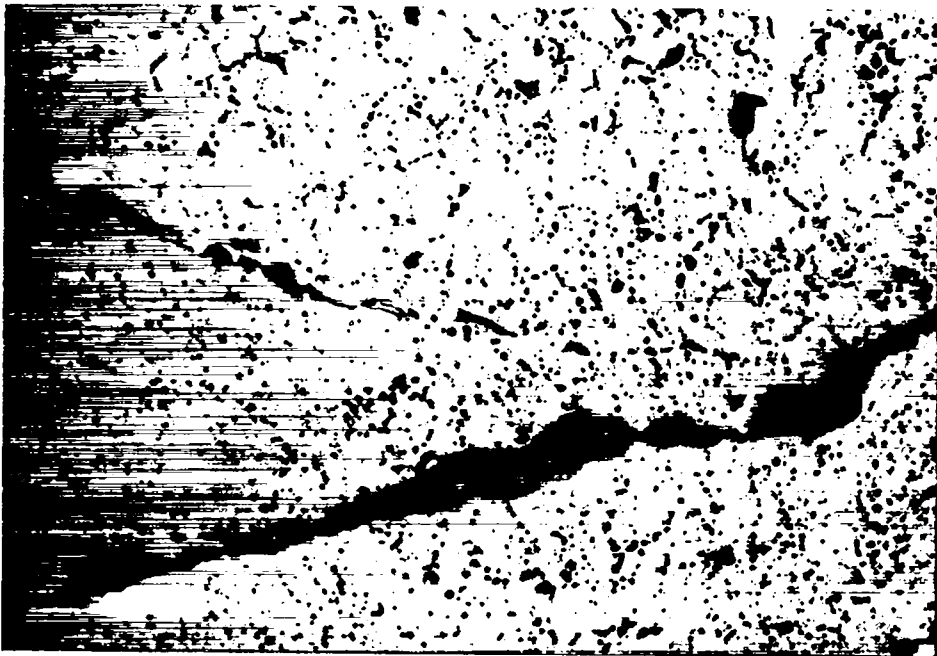*Polished cross section of specimen HPZ-115-12*
after annealing. (8X).

Fig. D-2.
Crack healing in HPZ-115-12. Note the string of porosity resulting from crack healing.
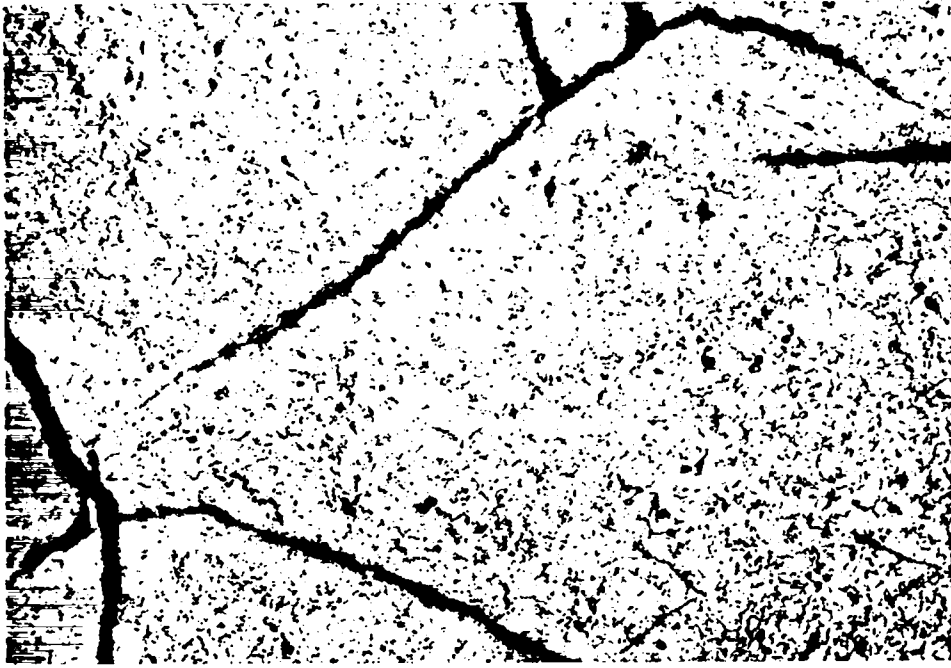*(200X).*

Fig. D-3.

Crack healing in HPZ-115-12. Note string of porosity and undulating shape of the crack after high-temperature exposure. (50X).
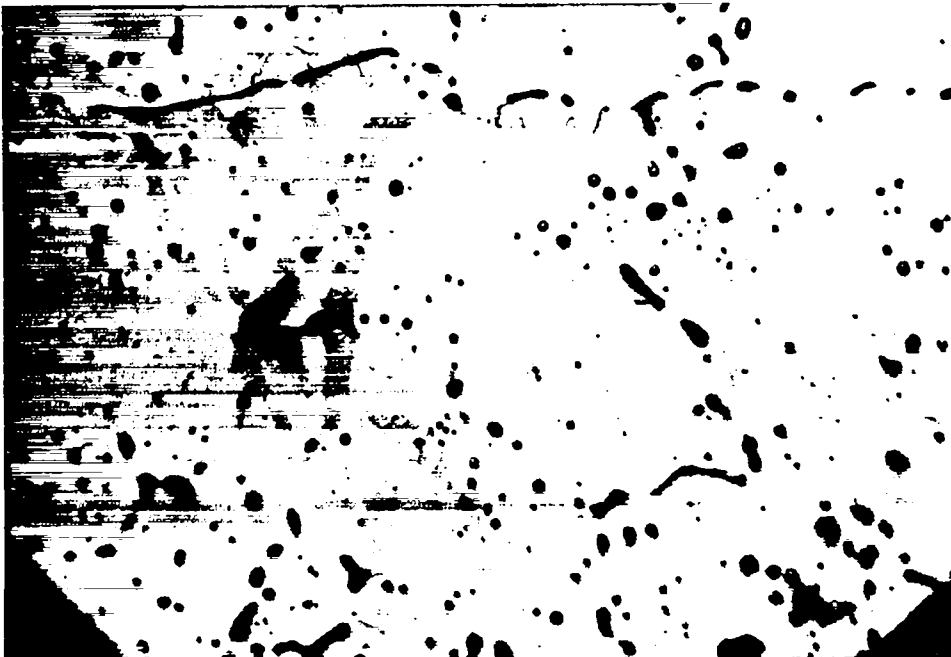

Fig. D-4.

Crack healing in HPZ-115-12. Note formation of elongated porosity as a result of crack healing, and formation of apparent grain boundary segment. Lath-like features are believed to be suboxide formation. (500X).
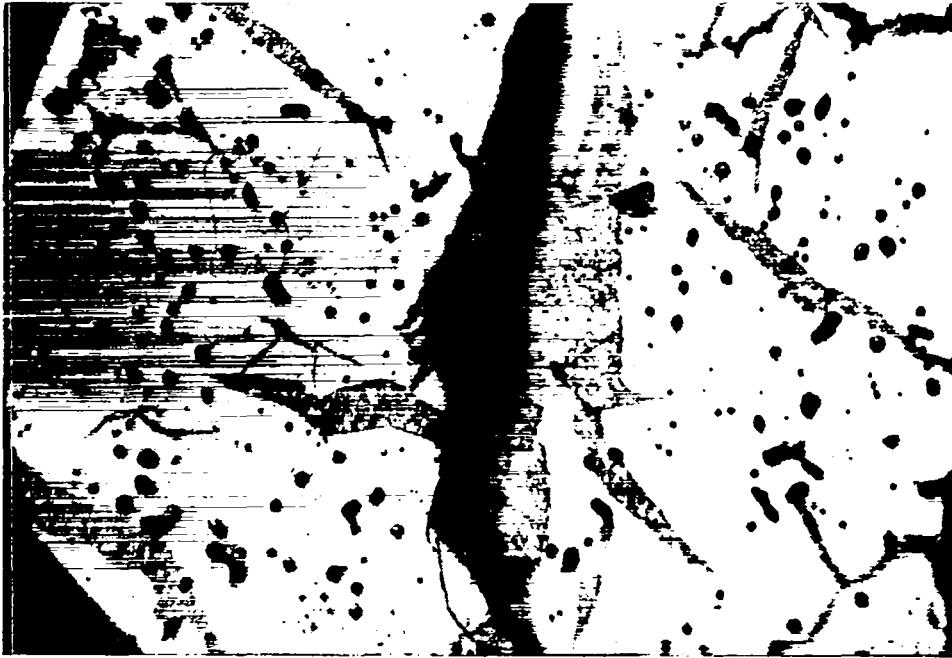
Fig. D-5.

Microstructure of specimen HPZ-115-12 after elevated-temperature exposure. Lath-like features are believed to be suboxide formation. Note sharp grain boundaries and absence of grain boundary helium voids. (500X).

APPENDIX E

EFFECT OF ANNEALING ON ^{238}PUO$_2$ FRACTURE SURFACES

Operation of diffusive processes in ^{238}PuO$_2$ is important to its elevated-temperature mechanical properties. Unfortunately, there is little diffusion data on ^{238}PuO$_2$ in the literature,[1] and none on plutonium diffusion in ^{238}PuO$_2$.

To gain insight into the temperature range where diffusion becomes significant in ^{238}PuO$_2$, as-fabricated specimen HPZ-115-4 was fractured at room temperature, and a suitable fractured shard was observed by REM. This shard was then annealed 30 min at 1000°C in vacuum, and the same fracture surface was replicated after being annealed. Then the shard was further annealed for 30 min at 1400°C and rereplicated. Finally, the shard was annealed 30 min at 1600°C, and replicated once again. The experiment was to determine the temperature range in which surface changes took place in ^{238}PuO$_2$, and the character of those changes. Such changes might indicate the operation of a diffusive mechanism.

Room temperature fracture surfaces were of two general types, rounded grains and transgranular cleavage. Examples are shown in Figs. E-1 and E-2. Rounded grain surfaces showed grain boundary grooving and a general absence of helium bubbles. We believe that such surfaces were not produced by room temperature fracture, but, rather, represent cracks produced during fabrication, and thus already exposed to high temperature. Thus, the surface morphology already exhibits effects of elevated temperature.

Fig. E-1.
Room temperature rounded grain fracture surface. (5000X).

Fig. E-2.
Room temperature transgranular cleavage fracture surface. (4000X)

Transgranular cleavage surfaces represent actual room temperature fracture of ^{238}PuO$_2$. Such surfaces showed distinct cleavage steps and internal porosity, with an absence of grain boundary definition. Thus, these surfaces would be expected to show the most marked effects of annealing, because they had not been exposed to elevated temperature before the annealing.

There were no obvious changes in either type of fracture surface after 30 min at 1000°C. Figure E-3 shows a cleavage surface after this exposure. However, after 30 min at 1400°C, "thermal swirls" on both the rounded grain and transgranular cleavage surfaces and the beginnings of grain boundary thermal etching and rounding off of cleavage steps on the transgranular cleavage surface were noted (Figs. E-4 and E-5). A transgranular cleavage surface after 30 min at 1600°C is shown in Fig. E-6.

The "thermal swirls" may represent thermal etching of crystallographic planes that intersect the surface topography. As the transgranular cleavage surfaces are annealed at higher temperatures, their features are being modified by diffision, so that they increasingly resemble the rounded grain surfaces.

It is interesting to compare the fracture surface annealing results with observations of grain growth in ^{238}PuO$_2$ resulting from elevated-temperature annealing, as the latter process is also diffusion controlled. Figures E-7 through E-11 show the microstructures of ^{238}PuO$_2$ specimens fabricated by hot pressing according to the scheme shown in Fig. 6 in the body of the report, and sintered at increasingly higher temperatures. The as-hot pressed material (Fig. E-7) displayed "ghost" substoichiometric features that made the grain size difficult to resolve. The as-hot-pressed grain size is estimated to be 5 μm. In a detailed grain growth study, Keenan et al.[2] reported 4-, 7-, 8-, and 26-μm grains for sintering temperatures of 1000, 1200, 1350, and 1527°C, respectively. Although there is no apparent grain growth at 1000°C, the "ghost" substoichiometric structure has disappeared. There is limited grain growth at 1200 and 1350°C and dramatic growth at 1527°C.

These microstructural observations indicate that some diffusive processes take place in ^{238}PuO$_2$ at temperatures as low as 1000°C and that they lead to substantial microstructural changes at temperatures above 1400°C.

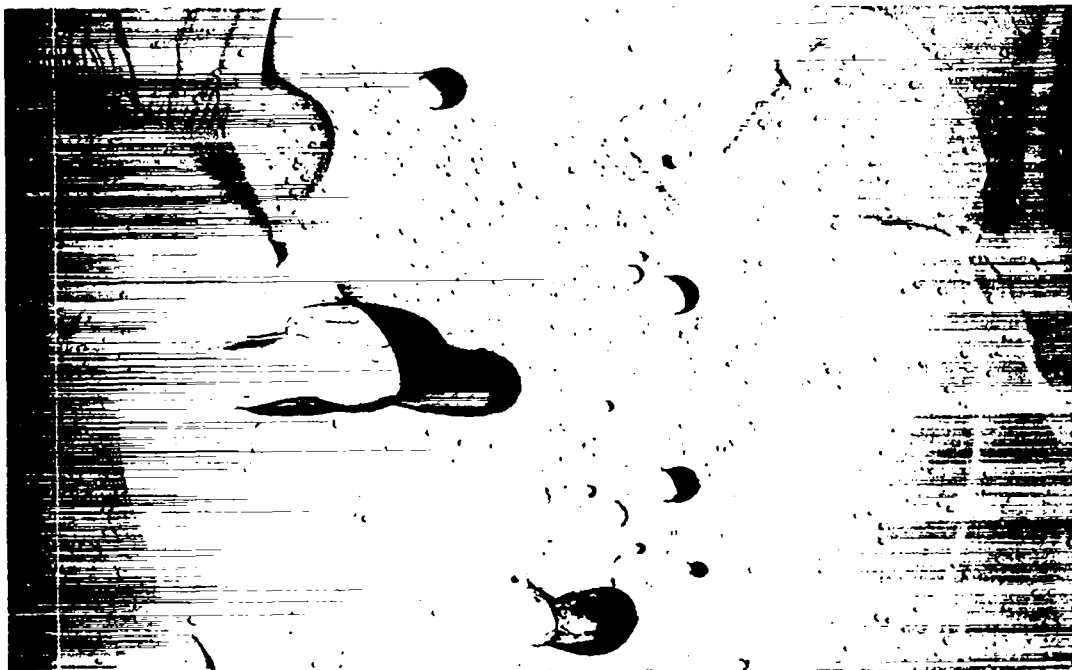*Fig. E-3.*
Transgranular cleavage fracture surface after 30-min 1000°C thermal exposure. (5000X).

Fig. E-4.

Rounded grain fracture surface after 30-min 1400°C thermal exposure. Note formation of thermal swirls. (4800X).
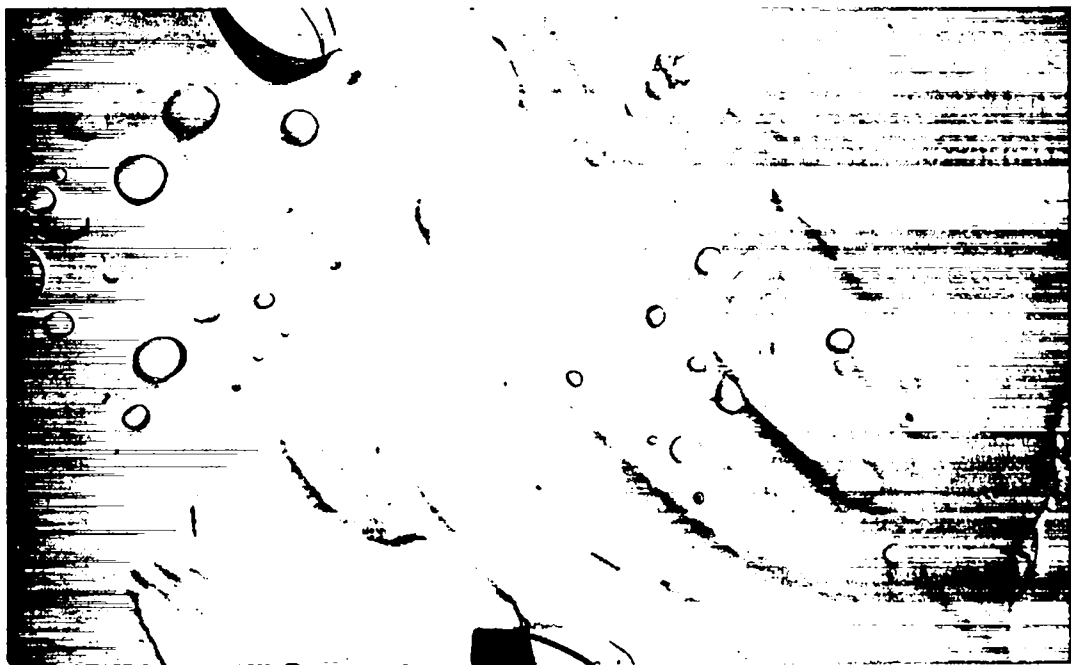

Fig. E-5.

Transgranular cleavage fracture surface after 30-min 1400°C thermal exposure. Note grain boundary thermal etching and rounding of cleavage steps. (5000X).
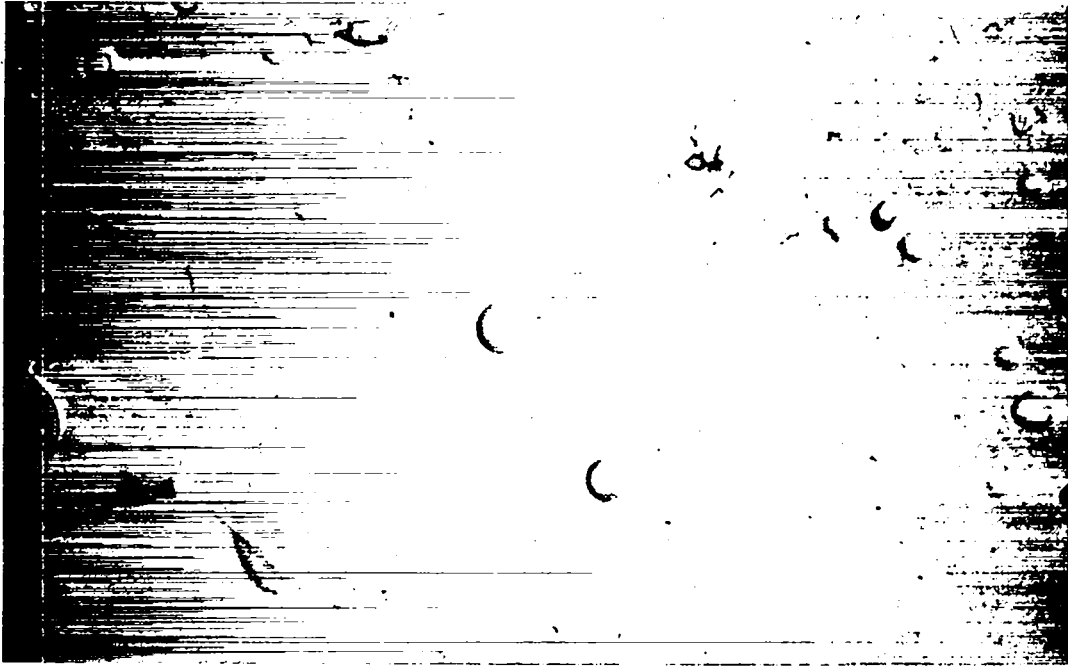
Fig. E-6.
Transgranular cleavage fracture surface after 30-min 1600°C thermal exposure. Note deeper grain boundary thermal etching, and cleavage step rounding. (4000X).
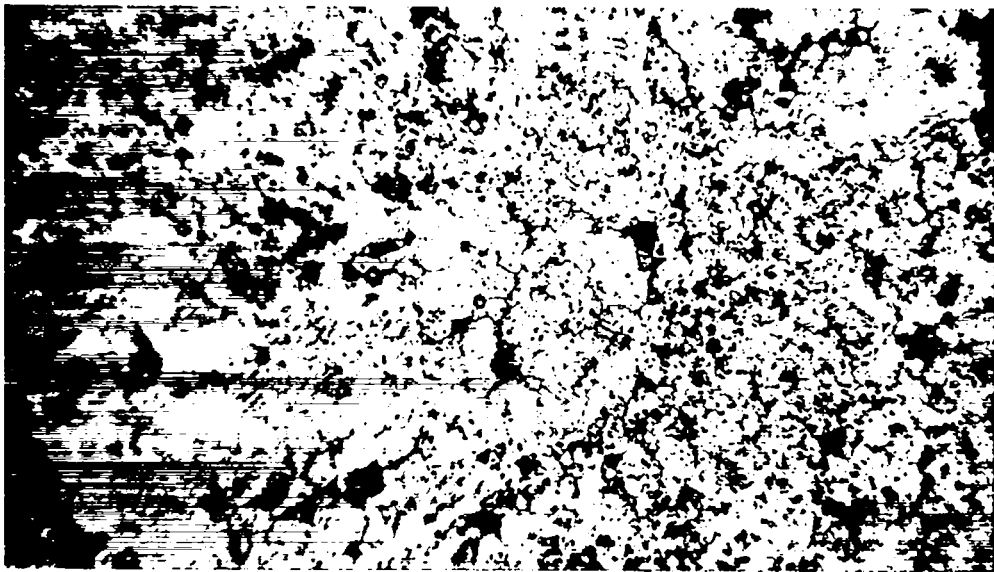

Fig. E-7.
As-hot pressed $^{238}PuO_2$ microstructure. Note substoichiometric "ghost" structure. (500X).
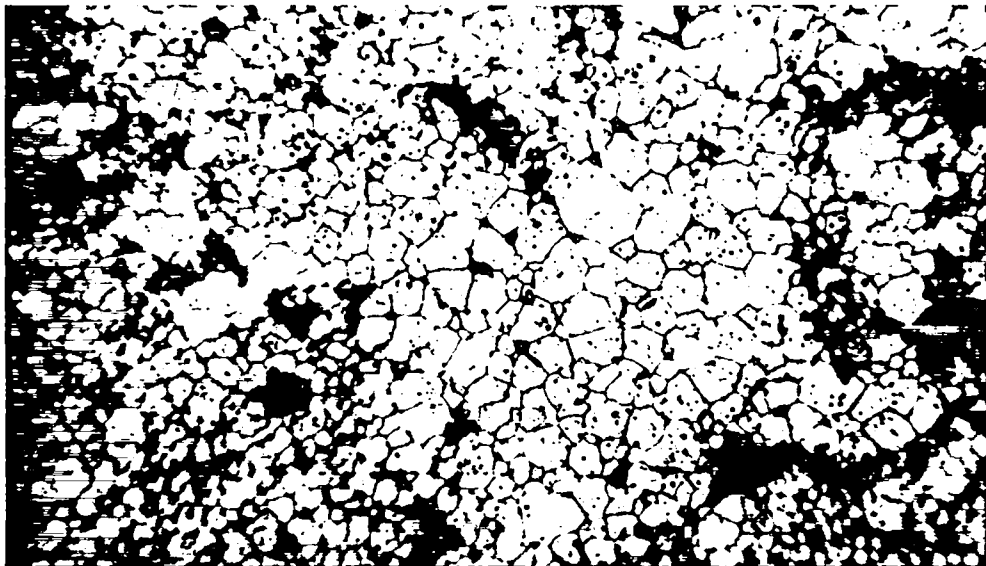
Fig. E-8.
Post hot pressing sinter at 1000°C. (500X).

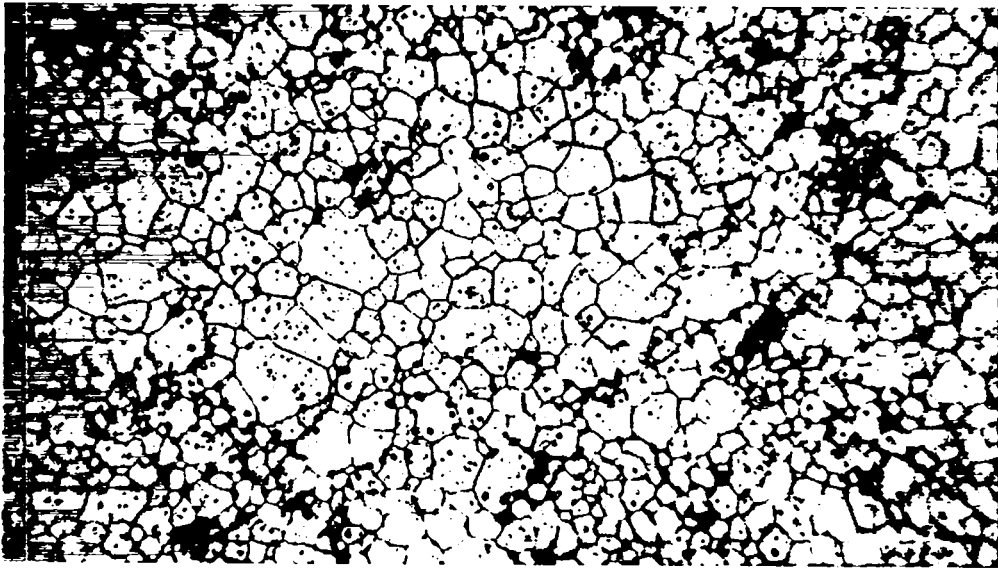*Fig. E-9.*
Post hot pressing sinter at 1200°C. (500X).

Fig. E-10.
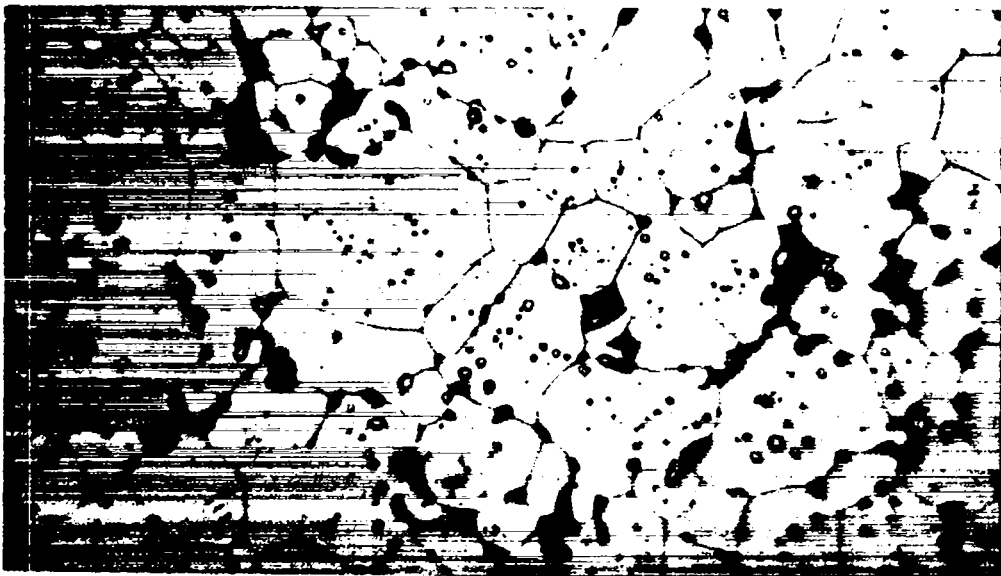*Post hot pressing sinter at 1350°C. (500X).*

Fig. E-11.
Post hot pressing sinter at 1527°C. (500X).

REFERENCES

1. R. L. Deaton and C. J. Weidenheft, "Self-Diffusion of Oxygen in $^{238}PuO_2$," J. Inorg. Nucl. Chem. **35**, 649-650 (1973).

2. T. K. Keenan, R. A. Kent, and R. W. Zocher, "The Relationship of Fabrication Parameters to Selected Properties of $^{238}PuO_2$ Radioisotope Fuels: I. Dimensional Changes, Stoichiometries and Microstructural Features," Los Alamos Scientific Laboratory report LA-5622-MS (May 1974).